J Mater Sci

Composites & nanocomposites

Sunlight-active defect-tuned g-C_3N_4@Zn-doped TiO_2 heterojunction photocatalyst immobilised onto cotton fabric for efficient pollutant degradation and antibacterial activity

Usman Zubair[1], Muhammad Zeshan Ali[1], Wasif Razzaq[1], and Zakariya Zubair[1,*]

[1] *Department of Materials, School of Engineering and Technology, National Textile University, Lahore-Sheikhupura Road, Faisalabad 37610, Pakistan*

Received: 22 June 2026
Accepted: 23 August 2026

ABSTRACT

Textile wastewater containing over 700 000 tonnes of synthetic dyes annually remains a major environmental challenge. Conventional photocatalysts suffer from rapid charge recombination, limited visible-light response, and poor recoverability. Here we report a sunlight-active, self-cleaning cotton fabric immobilised with a defect-tuned Zn@TiO2/g-C3N4 heterojunction. Defect-engineered g-C3N4 was prepared by optimising the melamine: cyanuric acid ratio, followed by ex situ ball milling with 0.5 mol% Zn-doped TiO2. The composite was covalently anchored onto cotton via GPTS. Under natural sunlight (1000 W m^{-2}), the fabric achieved 98 % methylene blue degradation in 90 min (pseudo-first-order k = 0.027 min^{-1}) and 99.96 % reduction of *E. coli* and S. aureus within 24 h. Hydroxyl radicals (HO•) were identified as the dominant reactive species. The coating increased fabric elongation to 21 % while preserving breathability. This scalable, zero-energy platform offers a practical route to self-cleaning textiles and solar-driven wastewater remediation.

GRAPHICAL ABSTRACT

A redesigned graphical abstract (aspect ratio 8:5) has been prepared. It follows one clear storyline: precursor defect regulation (melamine-cyanuric acid) → heterojunction construction by ball milling → GPTS-assisted fabric immobilisation → sunlight-driven ROS generation → simultaneous dye degradation and antibacterial action. The revised high-resolution graphical abstract is supplied as a separate file.

Handling Editor: Hanchao Zhang.

Address correspondence to E-mail: zzubair@ntu.edu.pk

https://doi.org/10.1007/s10853-026-13686-9
Published online: 07 September 2026

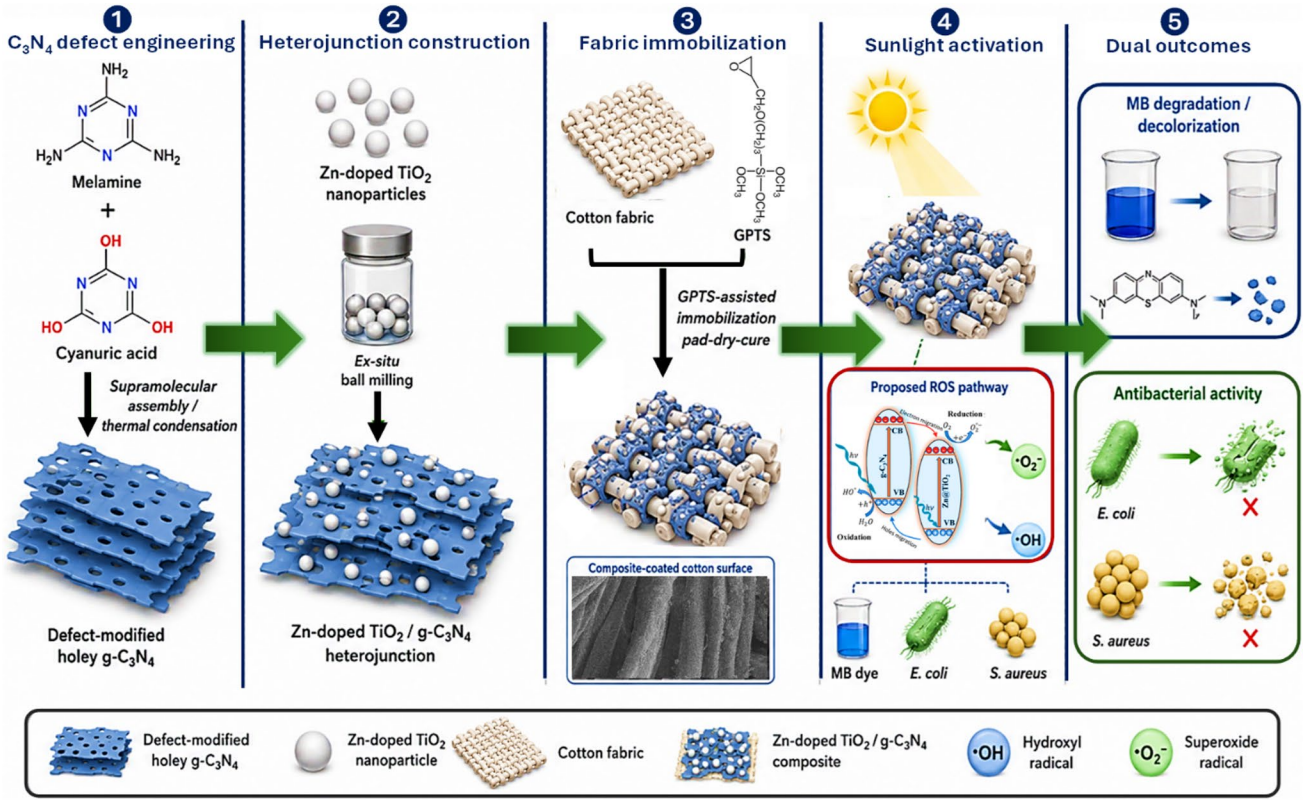

Introduction

The fashion and textile industry is one of the world's most polluting sectors, with dye-related wastewater posing a severe threat to global water resources. According to recent estimates from the United Nations Environment Programme (UNEP), the textile industry generates approximately 92 million tonnes of waste annually, much of which stems from production processes that have doubled in volume between 2000 and 2015 [1, 2]. This waste includes synthetic dyes, with global dye production exceeding 700000 tonnes per year, predominantly used in textiles, leading to widespread contamination [3]. The World Health Organization (WHO) and UN reports highlight that textile dyeing alone accounts for about 20% of global industrial water pollution, releasing untreated effluents laden with toxic azo dyes, heavy metals, and auxiliaries into rivers and oceans [4–6]. These pollutants such as azo dyes of methylene blue (MB) and methyl orange (MO) disrupt aquatic ecosystems by reducing dissolved oxygen levels, block sunlight penetration, and pose human health risks, including carcinogenicity, mutagenicity, and endocrine disruption [7–9]. As global textile consumption surges with estimation of 148 million tonnes by 2030 [10], the need to mitigate dye pollution has increased, driving the need for sustainable remediation technologies that align with UN Sustainable Development Goals, particularly SDG 6 (Clean Water and Sanitation) and SDG 12 (Responsible Consumption and Production).

Photocatalysis emerges as a promising green technology for harnessing solar energy to degrade organic wastewater pollutants into harmless byproducts [11–13]. At its core, photocatalysis involves a semiconductor catalyst that absorbs photons with energy equal to or greater than its bandgap (E_g), promoting electrons (e^-) from the valence band (VB) to the conduction band (CB), thereby generating electron–hole (e^-/h^+) pairs [14–18]. These charge carriers migrate to the catalyst surface, where holes oxidise water or hydroxide ions to produce hydroxyl radicals ($HO^\bullet$), and electrons reduce adsorbed oxygen to form superoxide radicals ($O_2^{\bullet-}$) or hydrogen peroxide (H_2O_2). These reactive oxygen species (ROS) then attack dye molecules, cleaving chromophore groups [19]. The

process follows first-order kinetics ($\ln(C_0/C_t) = k*t$) or second-order kinetics ($1/C_t - 1/C_0 = k*t$), where C_0 and C_t are initial and time-dependent dye concentrations, respectively, and k is the rate constant [20, 21]. Solar-driven photocatalysis is particularly advantageous, utilising the abundant visible spectrum (~45% of sunlight) to minimise energy costs and environmental footprints [19, 22].

Graphitic carbon nitride (g-C_3N_4), a metal-free polymeric semiconductor, offers inherent visible-light activity with a bandgap of ~2.7 eV [23]. Derived from nitrogen-rich precursors like melamine via thermal polymerisation, g-C_3N_4 features a layered structure similar to graphite, providing high thermal and chemical stability (up to 600 °C) and a large surface area useful for pollutant adsorption. Its CB and VB positions enable efficient water splitting and pollutant degradation under visible light, but pristine g-C_3N_4 suffers from low conductivity, low charge mobility, and high recombination rates of electron–hole (e^-/h^+) pairs [24]. This limitation leads to defect engineering of g-C_3N_4. On the other hand, titanium dioxide (TiO_2) is a wide bandgap material found in three crystalline forms of anatase (bandgap ~3.2 eV), rutile (~3.0 eV), and brookite (~3.3 eV). The anatase phase is particularly prevalent in photocatalytic applications, such as hydrogen evolution [25]. However, its UV-limited absorption (only ~5% of solar irradiation) restricts utilisation of visible light (~45% of solar irradiation) that severely hampers efficiency in sunlight-driven processes [26]. Additional challenges include mass transfer limitations on TiO_2 surfaces, low affinity for organic pollutants (especially hydrophobic ones), nanoparticle aggregation leading to reduced light penetration to active sites, and increased scattering in smaller particles that diminishes overall activity [27, 28]. To address these challenges, researchers have employed strategies such as: (a) modifying TiO_2 for visible-light responsiveness; (b) optimising synthesis for controlled crystal structure, reduced particle size, and enhanced pollutant affinity; and (c) developing recoverable second-generation catalysts. Among modifications, transition metal (TM) doping stands out as a cost-effective approach because TM ions, being multivalent with d-electron configurations, can introduce heterojunctions within the TiO_2 bandgap, inhibiting electron–hole recombination and extending photocatalytic performance into the visible spectrum. Cu- and Zr-doping may increase the bandgap to 3.7 eV and 3.5 eV, respectively, without capturing visible light and effecting dye degradation while Zn-doping induced a redshift, narrowing the bandgap from 3.2 to ~2.8 eV with broader absorption of visible light (400–700 nm), and charge transfer between impurity bands and TiO_2 conduction band which enhances ROS generation, particularly $HO^\bullet$ [29, 30]. Zn-doped TiO_2 further benefits from enhanced corrosion resistance, hardness, semiconducting, magnetic properties, transparency, electron mobility, increased surface-bound hydroxyl groups, and expanded surface area, making it highly effective for photocatalysis [26].

Although significant progress has been made in defect engineering of g-C_3N_4 to enhance its photocatalytic performance [31, 32], the majority of strategies remain focused on standalone or powder-form materials for applications such as hydrogen evolution or single-pollutant degradation in suspension. Such strategies include a supramolecular precursor approach by using melamine-urea mixtures have successfully produced holey g-C_3N_4 nanotubes via template-free thermal polymerisation [33], vacancy engineering (C/N-vacancies) through thermal treatment [34], gas templating (e.g. NH_4Cl) [31], sulphur sublimation [35], and photoassisted hydrazine etching [36]has been shown to enlarge surface area, narrow the bandgap, and create shallow trap states that improve charge separation. Other routes, including hard/soft templating (SiO_2, surfactants) [37, 38], NaClO wet etching for hierarchical pores [39], and thermal exfoliation [32], have further demonstrated the ability to introduce porosity and nitrogen vacancies, yet these methods often require additional templates, harsh etchants, high-energy post-treatments, and vacuum/atmosphere control which can limit the scalability and environmental friendliness [40, 41].

Recent literature [42–44]further underscores the importance of controlled defect chemistry and interfacial design which demonstrate that vacancy-rich and heterostructured g-C_3N_4 systems significantly outperform their pristine counterparts. In parallel, recent advances in solar-driven organic transformations [45, 46] highlight the growing maturity of sunlight photocatalysis for environmental applications.

Critically, there is a persistent gap in translating these defect-engineered g-C_3N_4 structures into scalable and fabric-integrated heterojunction photocatalysts for real-world textile wastewater remediation and self-cleaning textiles. To the best of our knowledge, no studies have combined ratio-optimised melamine-cyanuric acid supramolecular precursors with

transition metal-doped TiO_2 (e.g. Zn@TiO_2) through *ex situ* ball milling. While sol–gel, hydrothermal, and calcination routes dominate, ex situ ball milling remains untapped for such a hybrid system. Ball milling induces defects, reduces particle size, enhances interfacial contact, and promotes heterojunction formation without high temperatures, potentially improving charge transfer and stability. Few studies have applied it to analogous composites; for example, Zhu et al. prepared C_3N_4/TiO_2 hybrids via ball milling, reporting enhanced photocatalytic performance for rhodamine B degradation due to improved dispersion and interface [47]. More recently, Li et al. utilised ball milling to sensitise g-C_3N_4 with zinc phthalocyanine (ZnPc) and achieved superior visible-light activity for organic pollutant removal [48]. Recent literature underscores the potential of such composite systems, i.e. Arfa et al. demonstrated sunlight-driven photocatalytic fabrics immobilised with Zn-doped TiO_2 nanoparticles, achieving 96 % degradation of commercial dyes within 3 hours via a sol–gel synthesis and pad-dry-cure method. Their work highlighted h^+ as the dominant species in first-order kinetics ($k \approx 0.0087–0.0131\ min^{-1}$ for MB and MO) [26]. Similarly, Akhtar et al. reported a hydrothermally synthesised $AgBiS_2$/g-C_3N_4 binary composite that degraded ~93% MB in 180 minutes under sunlight, attributing efficiency to heterojunction-facilitated charge separation and bandgap reduction. These studies affirm the viability of doped and composite photocatalysts for dye remediation [49].

In this study, a heterojunction composite of Zn-doped TiO_2 with defect-induced g-C_3N_4 was developed by *ex situ* ball milling and is characterised for its structural, morphological, and optical properties, and the solar light-driven photocatalytic degradation of model dye MB is evaluated. We hypothesise that the synergistic combination of (i) nitrogen vacancies and hierarchical porosity generated by optimised melamine-cyanuric acid ratios, (ii) Zn-doping of TiO_2 to extend visible-light absorption, (iii) *ex situ* ball milling to create an intimate solid-state heterojunction that promotes directional charge separation, and (iv) covalent immobilisation of the composite onto cotton fabric via GPTS will collectively overcome the three long-standing limitations of conventional powder photocatalysts of rapid charge recombination, restricted visible-light utilisation, and poor catalyst recoverability which may enable efficient, sunlight-driven dye degradation, and antibacterial activity in textiles. Zn-doped TiO_2 was synthesised at 0.5% molar ratio using the sol–gel technique; defected g-C_3N_4 was realised using thermal condensation by mixing cyanuric acid at different ratios with melamine. The composite catalyst is immobilised onto the cotton fabric surface using a silane coupling agent, 3-glycidoxypropyl trimethoxysilane (GPTS). SEM, XRD, Raman, and FTIR are employed for the detailed analysis of the as-developed composite. Photocatalytic performance is assessed along with kinetic study and radical scavenging experiments to elucidate the mechanism of dye degradation. The surface- and defect-engineered heterojunction organic and inorganic hybrid photocatalyst has proved to be an effective strategy for sunlight photodegradation.

Materials and methods

Synthesis of defective graphitic carbon nitride (g-C_3N_4) with Zn-doped TiO_2

All chemicals were used as received. Melamine (99 %, Sigma-Aldrich), cyanuric acid (98 %, Sigma-Aldrich), titanium(IV) isopropoxide (97 %, Aldrich), zinc acetate dihydrate (99.9 %, Alfa Aesar), 3-glycidoxypropyltrimethoxysilane (GPTS, 98 %, Aldrich), isopropanol (HPLC grade, Merck), and methylene blue (analytical grade, Merck) were employed.

The graphitic carbon nitride (g-C_3N_4) was developed through direct thermal condensation. In the ceramic crucible, 10 g of melamine was taken and directly heated in a muffle furnace at 550 °C for 3 h by adjusting the heating rate of 5 °C/min in air. The required product was cooled and ground into a fine powder using a mortar and pestle for further use. It was labelled as GCN-1:0 (pure melamine). Defected g-C_3N_4 was prepared by following the above strategy but varying the concentration of melamine and cyanuric acid as starting precursors, such as GCN-1:1 (1 part melamine to 1-part cyanuric acid), GCN-2:1 (2 parts melamine to 1-part cyanuric acid), GCN-3:1 (3 parts melamine to 1-part cyanuric acid), and GCN-4:1 (4 parts melamine to 1-part cyanuric acid). Zn-doped TiO_2 at a 0.5% molar ratio is prepared using the sol–gel technique as per the procedure in our previous research [26]. Each formulation of g-C_3N_4 was mixed with Zn-doped TiO_2 nanoparticles and ball milled at a rpm of 500 for 6 hours. This *ex situ* treatment of g-C_3N_4 with nanoparticles developed Zn@TiO_2/g-C_3N_4

composites with improved surface area and electronic properties, much needed for photocatalysis-based dye degradation. For functionalisation of the nanocomposite, 6% of g-C_3N_4@Zn-doped TiO_2 on the weight of the fabric was dispersed into 100 mL of isopropanol and ultrasonicated for 1 hr. After this, 125% of GPTS on the weight of the nanocomposite was added, followed by the adjustment of the solution pH to 4.5 using 0.01 M HCl. The solution was refluxed afterwards at 60 °C for 4 hrs. Immobilisation of functionalised nanocomposite was done by dipping the fabric into GPTS functionalised nanocomposite solution and rolling the fabric by padder machine, and then, the fabrics were dried at 100 °C and cured at 150 °C for 3 minutes in a Stenter Frame (pin TC-M-28).

Compared with conventional sol–gel, hydrothermal/calcination routes, ex situ ball milling confers several distinct structural advantages: (i) it generates intimate solid-state interfacial contact between Zn@TiO_2 and defect-engineered g-C_3N_4 without high-temperature sintering that could destroy the holey morphology; (ii) mechanical energy introduces additional surface defects and reduces crystallite size, increasing active-site density; (iii) it avoids residual solvents/templates that may poison active sites; and (iv) the process is scalable, solvent-free and energy efficient.

Characterisation of the catalyst components and functionalised fabric

Photocatalysts were characterised by FTIR-ATR (PerkinElmer-FTIR spectrometer), SEM (Nova Nano SEM), Raman spectrometer (Optosky Raman Microscope with laser power of 2 mW), and XRD (X-ray powder diffractometer, having Cu kα as a radiation source (λ = 0.154 nm). Tensile properties (tensile strength with elongation) were measured by UTM under ISO 13934-1:2014, and fabric comfort analysis was performed by measuring water vapour permeability (under BS 7209:1990) and vertical wicking (under AATCC 197:2018). The antibacterial potential of Zn@TiO_2/g-C_3N_4 composite-coated fabric was evaluated against two common pathogens: *Staphylococcus aureus* (ATCC 6538) as Gram-positive and *Escherichia coli* (ATCC 25922) as Gram-negative. The bacterial counts were made just after contaminating the respective fabric with bacteria (t = 0 h) and 24 h after the incubation period (t = 24 h). The washing durability of up to 10 cycles of coated fabric was tested under the ISO 105 C03 method.

The operation details of some characterisation items can be referred to the literature [50–54]. For electrochemical impedance spectroscopy, the active materials are coated onto the FTO working electrode; a Pt wire is taken as the counter electrode, Ag/AgCl as the reference electrode, and 0.1 M Na_2SO_4 solution as an electrolyte. The EIS is performed on Corrtest electrochemical workstation in the frequency range of 100 kHz to 0.1 Hz, with a perturbation voltage of 5 mV under visible light, and the results are recorded as Nyquist plots. Photoluminescence (PL) spectra were recorded for the photoactive powder materials at room temperature using a F-7000 fluorescence spectrophotometer. The excitation wavelength was 380 nm, and all other parameters were kept constant to avoid any change due to test parameters. XRF analysis of the solid-state samples was performed on a JSX-1000S X-ray fluorescence spectrophotometer (JEOL, Japan).

Photocatalytic potential study of the composite

The photocatalytic potential of the g-C_3N_4 and Zn@TiO_2/g-C_3N_4 composites for methylene blue (MB) dye degradation was assessed under natural sunlight (1000 ± 100 W m^{-2}, 88 000 ± 3000 lux) and, for validation, under a calibrated solar simulator (AM 1.5G, 1000 W m^{-2}). All experiments were performed in triplicate; error bars represent standard deviation. MB dye solution with a concentration of 10 ppm and a volume of 100 mL was used for analysis. Typically, 40 mg of the composite was added to 100 mL of MB solution, and the pH was adjusted using 0.1 M HCl or NaOH. Beakers were stirred in the dark for 30 minutes on an orbital shaker to establish adsorption–desorption equilibrium, and the solution concentration was measured via a spectrophotometer. Then, the mixture was exposed to sunlight at 1000 W/m^2 (88000 ± 2000 Lux measured by a lux meter) in 250-mL borosilicate beakers on an orbital shaker at 200 rpm. Aliquots of 5 mL were sampled every 30 minutes and centrifuged, and the absorbance was recorded at 664 nm (specific for MB dye) to calculate the degradation percentage following Eq. (1) [55].

$$\text{Degradation}\% = 1 - \left(\frac{C_t}{C_0}\right) \times 100 \quad (1)$$

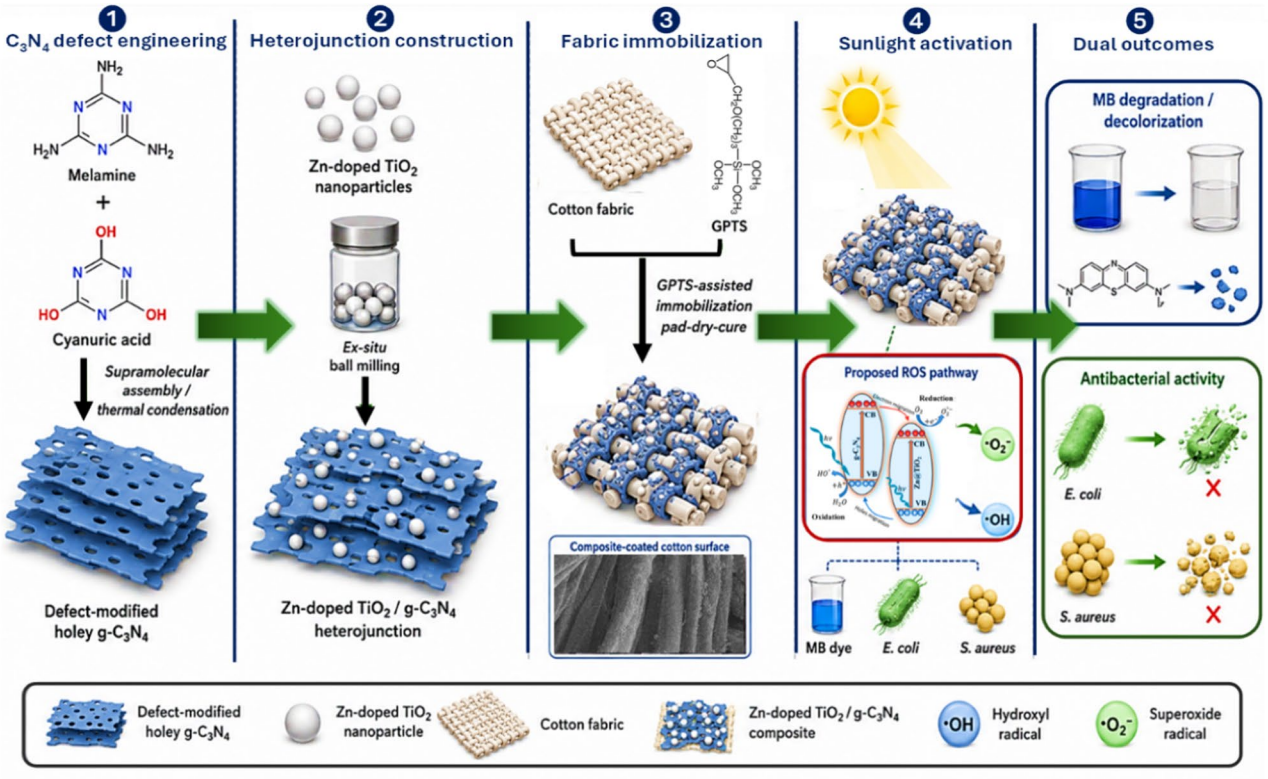

Scheme 1 Development of exfoliated holey g-C_3N_4, ex situ ball milling with Zn-doped TiO_2 to develop composite of Zn@TiO_2/g-C_3N_4, which degrades MB dye through photocatalysis.

Results and discussion

This research presents a scalable synthesis protocol to transform low-cost melamine, cyanuric acid, and Zn-doped TiO_2 into a sunlight-powered, self-cleaning cotton fabric. Stacked g-C_3N_4 exfoliates due to cyanuric acid and is ex situ ball milled with Zn-doped TiO_2 to develop a Zn@TiO_2/g-C_3N_4 composite, which is coated onto cotton fabric using GPTS and generates hydroxyl radicals ($HO^{\bullet}$) upon sunlight to degrade MB dye for a self-cleaning textile, as shown in Scheme 1. Scheme 1 explicitly illustrates: (i) supramolecular self-assembly of melamine and cyanuric acid precursors leading to defect-tuned holey g-C_3N_4, (ii) sol–gel synthesis of Zn-doped TiO_2 nanoparticles, (iii) ex situ ball milling for intimate heterojunction formation, (iv) GPTS-assisted covalent immobilisation onto cotton fabric, and (v) the subsequent sunlight-driven generation of reactive oxygen species (primarily HO•) responsible for methylene blue degradation and antibacterial action.

In a single thermal step, melamine polymerised into pristine g-C_3N_4, while controlled addition of cyanuric acid yields defected g-C_3N_4 featuring abundant surface -OH groups and an exfoliated structure, as shown in Fig. 1(a). Addition of Zn-doped TiO_2 (Fig. 1-b) into g-C_3N_4 through *ex situ* planetary ball milling resulted in composite of Zn@TiO_2/defectedg-C_3N_4 as shown in Fig. 1(c). One-step pad-dry-cure coating deposits the composite onto cotton fabric as shown in Fig. 1(d-e), yielding a flexible, breathable, self-cleaning textile that harnesses visible sunlight to generate massive flux of hydroxyl radicals ($HO^{\bullet}$) to degrade dye while sterilising itself against *E. coli* and *S. aureus*.

Physicochemical characterisation of the photocatalyst and related components

The FTIR spectra of the synthesised g-C_3N_4 and its defective variants (Fig. 2) provide critical insights into the chemical structure and modifications induced by the incorporation of cyanuric acid with melamine. The pristine g-C_3N_4 sample (1:0) exhibits characteristic peaks indicative of its triazine/heptazine framework at 810 cm^{-1}, C=N and C–N stretching vibrations in the range of 1200-1700 cm^{-1}, C–H stretching at 2900 cm^{-1}, and N–H stretching at 3000-3200 cm^{-1}, as shown

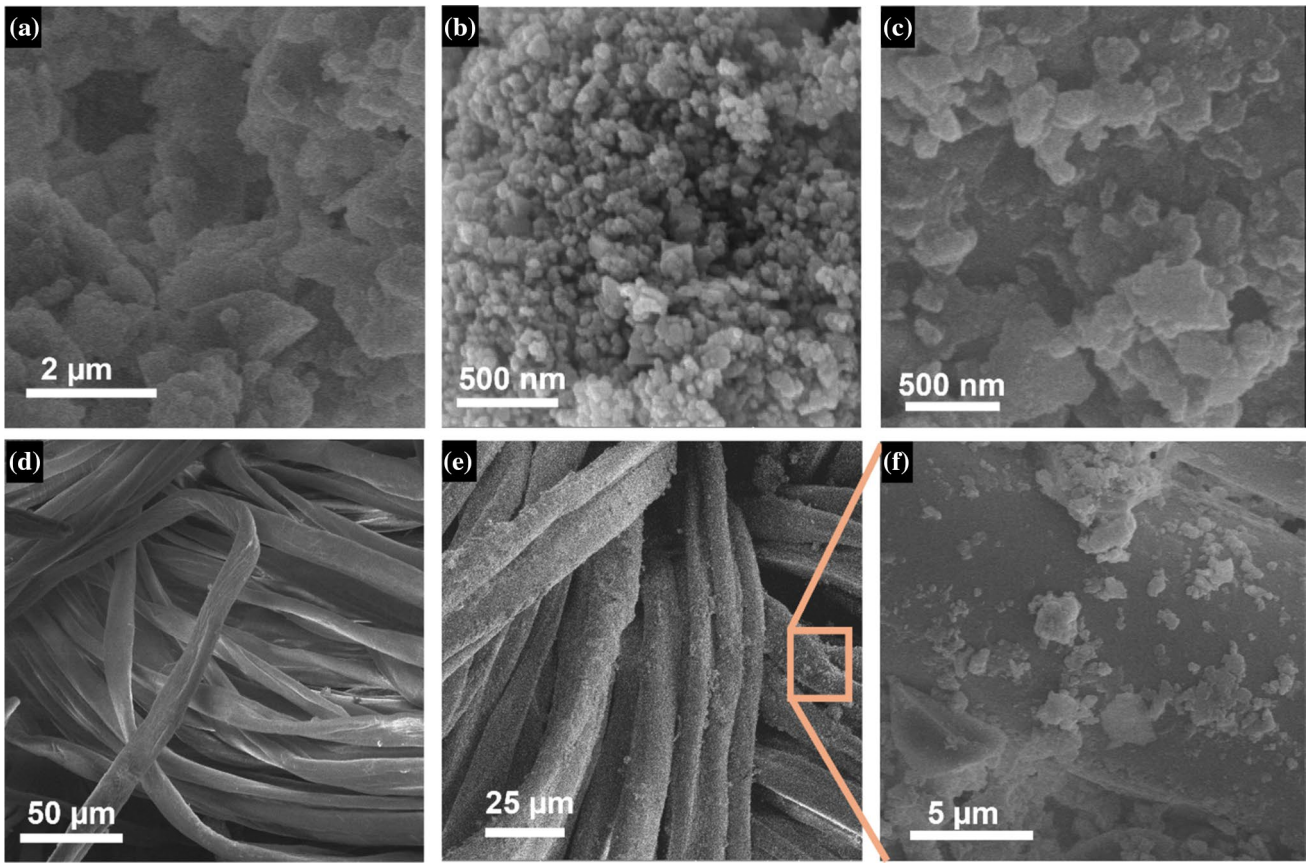

Figure 1 SEM images of **a** defected g-C_3N_4, **b** Zn@TiO_2 nanoparticles, **c** composite of Zn@TiO_2/defected g-C_3N_4, **d** only carbon fabric, **e** Zn@TiO_2/defected g-C_3N_4 composites-coated cotton fabric, and **f** zoomed-out morphology of Zn@TiO_2/defected g-C_3N_4 composites-coated cotton fabric.

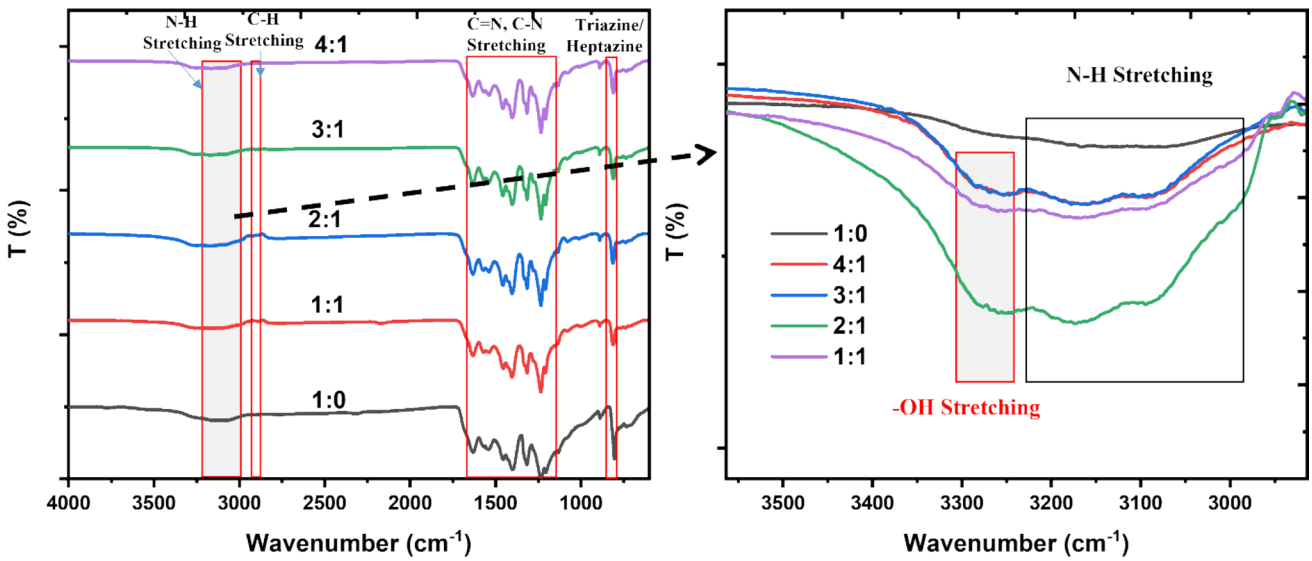

Figure 2 FTIR of g-C_3N_4 by pure melamine (1:0) and cyanuric acid doped melamine, where the right pane is the zoomed-in part of FTIR from 2900 to 3600 cm^{-1}.

in Fig. 2 (Left pane). These features confirm the successful formation of the polymeric g-C_3N_4 structure, consistent with its synthesis via thermal polymerisation of melamine. The development of defected g-C_3N_4 through the reaction of melamine with cyanuric acid is evidenced by the emergence of –OH stretching vibrations at ~3250 cm^{-1} in the doped samples (4:1, 3:1, 2:1, and 1:1), as zoomed in Fig. 2 (Right pane). This peak is absent in the pure melamine-derived g-C_3N_4 (1:0), indicating the introduction of hydroxyl groups due to the oxygen-containing cyanuric acid. The presence of these –OH groups enhances the material's hydrophilicity and potential for surface reactions, which enhance photocatalytic activity.

Notably, the C=O stretching vibrations around 1700 cm^{-1}, a characteristic peak expected from the carbonyl group of cyanuric acid, are absent. This finding aligns with results reported by other researchers [56] and may be due to decomposition or rearrangement of the cyanuric acid carbonyl groups, converting them into other oxygen-containing functionalities (e.g. -OH) during the thermal polymerisation process performed at the high temperatures (typically 500–600°C), or the strong hydrogen bonding and condensation reactions between melamine and cyanuric acid during synthesis could result in the loss of the carbonyl group through cyclisation or dehydration, forming a more stable triazine/heptazine structure without a distinct C=O signature. This is consistent with the observed retention of triazine/heptazine vibrations and the absence of new carbonyl-related peaks. The absence of C=O stretching suggests that the oxygen introduced by cyanuric acid primarily enhances the surface hydroxyl groups and defects, which are known to facilitate the generation of $HO^{\bullet}$ radicals for photocatalytic dye degradation [26].

The FTIR spectra of TiO_2 nanoparticles and Zn@TiO_2 showed characteristic peaks of metal-O stretching at 750 cm^{-1}, C–H stretching at 2900 cm^{-1}, bound water O–H bending and stretching at 1540–1680 cm^{-1} and 3200–3500 cm^{-1}, respectively, as shown in Fig. 3(a). The emergence of a Zn-Ti bond peak at 1410 cm^{-1} in Zn@TiO_2 confirms successful Zn doping, indicating substitution into the TiO_2 lattice and the introduction of defect states that enhance visible-light absorption.

Fig. 3(b) compares the FTIR spectra of Zn@TiO_2, uncoated cotton, and Zn@TiO_2/defected g-C_3N_4-coated cotton. The coated fabric retains Zn@TiO_2 characteristics, including M-O stretching at 750 cm^{-1}, C–H stretching at 2900 cm^{-1}, and O–H bending and stretching at 1540-1680 cm^{-1} and 3200-3500 cm^{-1}, respectively, confirming the presence of the photocatalytic composite. Additionally, peaks associated with uncoated cotton are observed, such as C–O–C stretching from cellulosic polymers at 1030 cm^{-1} and O–H stretching from hydrogen bonds in cellulose at 3200-3500 cm^{-1}, indicating that the coating preserves the fabric's native structure while integrating the Zn@TiO_2/defected g-C_3N_4 layer. The overlapping O–H regions suggest

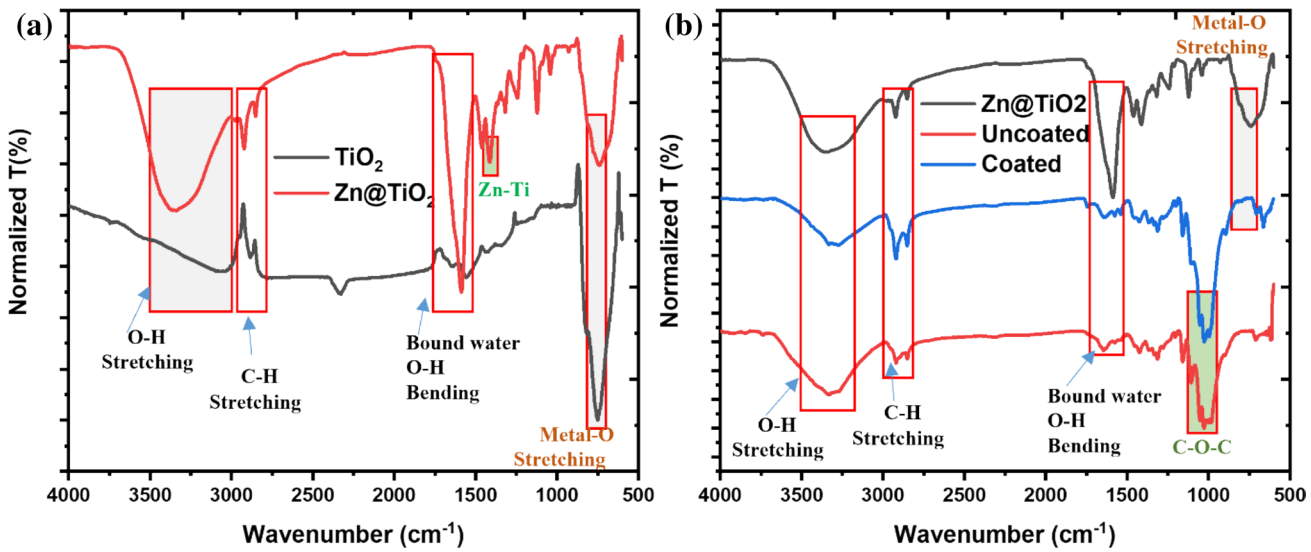

Figure 3 FTIR of **a** TiO_2- & Zn-doped TiO_2 nanoparticles and **b** FTIR of Zn@TiO_2, uncoated cotton, and Zn@TiO_2/g-C_3N_4-coated cotton.

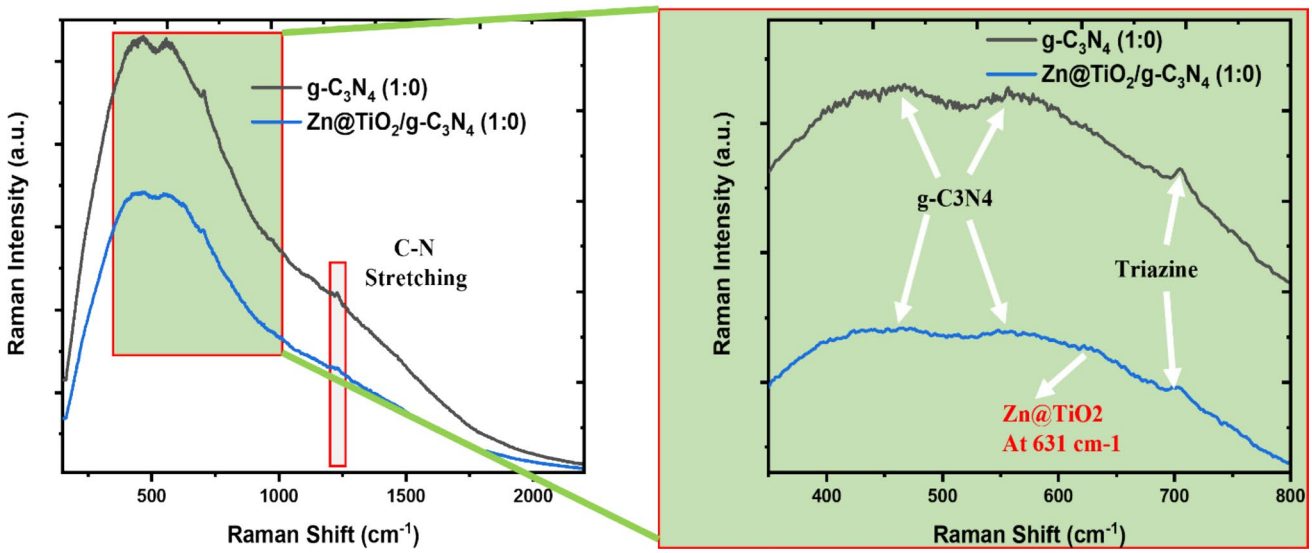

Figure 4 Raman spectra of g-C_3N_4 and Zn@TiO_2/g-C_3N_4.

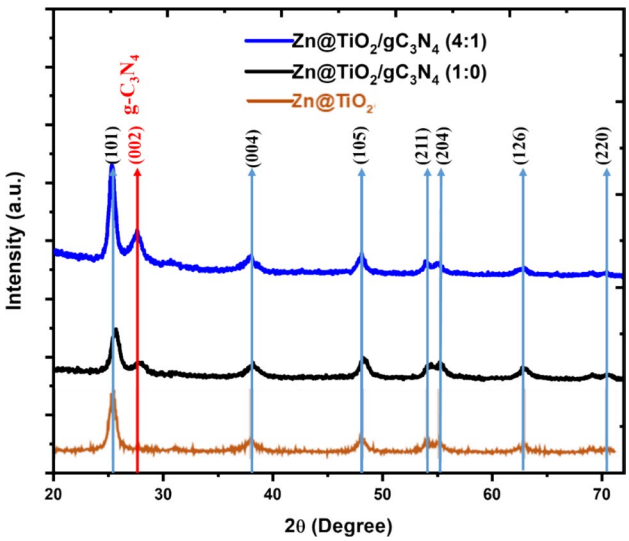

Figure 5 XRD patterns of Zn@TiO_2 and Zn@TiO_2/g-C_3N_4 (4:1) and Zn@TiO_2/g-C_3N_4 (1:0).

potential hydrogen bonding between the coating and cellulose, enhancing interfacial adhesion. These FTIR results adequately verify the successful synthesis of Zn@TiO_2 and its integration into the coated cotton fabric.

The Raman spectrum of the Zn@TiO_2/g-C_3N_4 composite confirms successful heterojunction formation through distinct vibrational modes of both components of Zn@TiO_2 and g-C_3N_4, as shown in Fig. 4. Zn@TiO_2/g-C_3N_4 showed a peak at 631 $cm^{-1,}$ which is missing in the spectra of g-C_3N_4. This characteristic peak at 631 cm^{-1} corresponds to anatase TiO_2, attributed to symmetric stretching of Ti-O bonds, with a slight blue shift from the typical 639 cm^{-1} due to Zn doping-induced lattice distortion and oxygen vacancies [57]. This shift supports enhanced electron trapping and visible-light responsiveness. Peaks at 468 cm^{-1} and 559 cm^{-1} are assigned to in-plane bending vibrations of C–N–C and N–C=N bonds in the heptazine units of g-C_3N_4, respectively [58], confirming the retention of its polymeric framework. The triazine ring breathing mode at 705 cm^{-1} is a hallmark of g-C_3N_4 structural integrity, arising from symmetric in-plane deformation of the heptazine ring [59]. Additionally, the C–N stretching vibration at 1240 cm^{-1} reflects the heterocyclic C–N network [60], further validating Zn@TiO_2/g-C_3N_4 composite formation. The coexistence of these well-defined TiO_2 and g-C_3N_4 modes, without significant overlap or suppression, demonstrates intimate interfacial contact achieved via *ex situ* ball milling, promoting charge transfer for efficient ROS ($HO^{\bullet}$ and $O_2^{\bullet-}$) generation.

The XRD patterns of pristine Zn@TiO_2 and Zn@TiO_2/g-C_3Ns_4 composites with different g-C_3N_4 precursors of 1:0 (pure melamine-based) and 4:1 (melamine: cyanuric acid ratio) were analysed to elucidate phase composition and structural interactions (Fig. 5). Pristine Zn@TiO_2 exhibits characteristic diffraction peaks at 2θ = 25.2°, 37.9°, 48.0°, 53.8°, 55.0°, 62.8°, and 70.1°, corresponding to the (101), (004), (105), (211),

(204), (126), and (220) planes of the anatase phase (JCPDS No. 89–4921) [61]. This confirms high-phase purity and crystallinity, with no rutile or brookite impurities, aligning with its wide bandgap and UV-dominant photocatalytic properties.

In the Zn@TiO_2/g-C_3N_4 (1:0) composite, the anatase TiO_2 peaks are retained, indicating that Zn doping and compositing do not alter the TiO_2 phase. However, an additional peak emerged at ~27.9°, attributed to the (002) plane of g-C_3N_4, reflecting interlayer stacking of its graphitic sheets [49]. For the Zn@TiO_2/g-C_3N_4 (4:1) composite, the anatase peaks persist, alongside a g-C_3N_4 (002) peak at 27.67°. The minor shift to a lower angle compared to the 1:0 composite may result from oxygen incorporation via cyanuric acid, expanding the interlayer spacing in defected g-C_3N_4. This peak confirms the successful incorporation of melamine-derived g-C_3N_4, with a slight shift from the standard ~27.4°, possibly due to structural interactions at the heterojunction interface or strain induced by ball milling synthesis. The absence of new Zn-related phases suggests substitutional doping of Zn^{2+} into the TiO_2 lattice because of the similar ionic size of Zn^{2+} and Ti^{4+}, suggesting Zn doping does not alter the crystal structure but creates defect states that narrow the bandgap without phase transformation. Overall, the FTIR, Raman, and XRD results validate the successful integration of Zn@TiO_2 and g-C_3N_4 to form the composites for visible-light photocatalysis.

Electrochemical impedance spectroscopy was employed to investigate the interfacial charge transfer behaviour of Zn-doped TiO_2, defect-modified g-C_3N_4 (4:1), and the Zn-doped TiO_2/g-C_3N_4 (4:1) heterojunction photocatalysts under visible light (Fig. 6). The Nyquist plots exhibited depressed semicircular regions at high-to-intermediate frequencies followed by rising tails at lower frequencies, where the semicircular diameter is mainly associated with charge transfer resistance at the photoelectrode/electrolyte interface, while the low-frequency response may arise from ion diffusion, surface adsorption, and transport through the porous catalyst layer. Among the tested photocatalysts, the Zn-doped TiO_2/g-C_3N_4 (4:1) heterojunction showed the smallest semicircular diameter, indicating the lowest apparent charge transfer resistance and the most efficient interfacial carrier transport, whereas defect-modified g-C_3N_4 (4:1) exhibited an intermediate response and Zn-doped TiO_2 showed the largest impedance. This trend suggests that controlled defect modification improves the electronic transport properties of g-C_3N_4, while its integration with Zn-doped TiO_2 further facilitates the migration and separation of photogenerated charge carriers across the heterojunction interface. The reduced resistance of the composite may be attributed to the intimate interfacial contact produced by ex situ ball milling, which

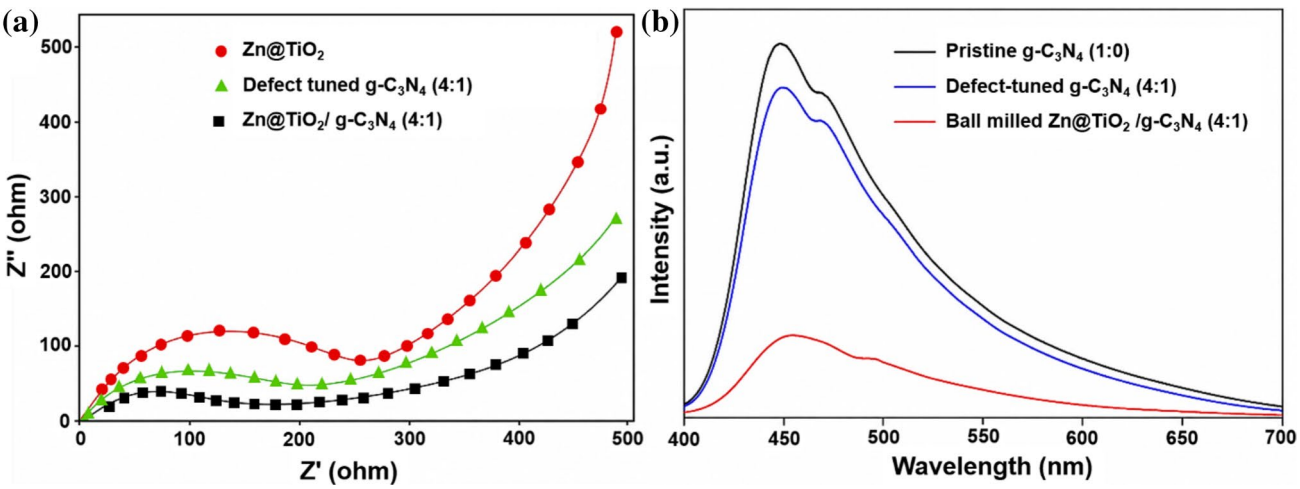

Figure 6 **a** Nyquist plots of Zn-doped TiO_2, defect-tuned g-C_3N_4 (4:1), and the Zn-doped TiO_2/g-C_3N_4 (4:1) heterojunction photocatalysts recorded under visible-light irradiation, **b** PL spectra of pristine g-C_3N_4 (1:0), defect-modified g-C_3N_4 (4:1), and the Zn-doped TiO_2/g-C_3N_4 (4:1) heterojunction.

provides additional pathways for carrier transfer and suppresses interfacial charge accumulation and recombination. The enhanced charge transfer behaviour observed for the heterojunction is therefore consistent with its improved photocatalytic activity.

The photoluminescence spectra of pristine g-C_3N_4 (1:0), defect-modified g-C_3N_4 (4:1), and the Zn-doped TiO_2/g-C_3N_4 (4:1) heterojunction are shown in Fig. 6b. All samples exhibit a broad emission band centred at approximately 440–450 nm, which is attributed to radiative recombination of photogenerated charge carriers within the conjugated heptazine framework of g-C_3N_4. Pristine g-C_3N_4 shows the highest PL intensity, indicating comparatively rapid electron–hole recombination. The reduced emission intensity of defect-modified g-C_3N_4 (4:1) suggests that precursor-induced structural defects introduce carrier-trapping and transport sites that suppress radiative recombination. A further pronounced PL quenching is observed for the Zn-doped TiO_2/g-C_3N_4 (4:1) composite, consistent with interfacial transfer of photogenerated carriers between the coupled semiconductor components and improved spatial charge separation across the heterojunction. These PL results, when considered together with the lower EIS charge transfer resistance and enhanced photocatalytic activity, support improved carrier utilisation in the optimised heterojunction.

Photocatalytic degradation performance of g-C_3N_4 and Zn@TiO_2/g-C_3N_4 catalyst

The effect of cyanuric acid with melamine to develop different formulations of 1:0 (pure melamine), 4:1, 3:1, 2:1, and 1:1 was directly analysed to determine the impact of cyanuric acid during thermal polymerisation. The g-C_3N_4 (1:0) exhibited 62.7% degradation at 60 min and 79% at 120 min (Fig. 7-a) due to its narrow bandgap (~2.7 eV) to capture visible light and generation of reactive ROS to degrade MB dye. Cyanuric acid-modified g-C_3N_4 (4:1) showed the highest degradation (68.8% at 60 min and 89.1% at 120 min) due to optimum surface defects caused by oxygenated cyanuric acid, which act as optimum charge traps for electron–hole pair separation with lower charge recombination, leading to a higher number of reactive ROS for dye degradation. As cyanuric acid increased from (4:1 to 1:1), degradation decreased from 68 to 40.4 % at 60 min and decreased from 89 to 75.5 % at 120 min. This decreasing trend stems from overwhelming oxygenated defects, through increasing concentration of cyanuric acid, that act as charge deep traps with localised states by becoming recombination centres where charges recombine non-radiatively with opposite carriers and lead to a lower number of reactive ROS for dye degradation. The catalyst with a 4:1 ratio of melamine to cyanuric acid showed peak degradation of 69 % and 89 % at 60 min and 120 min, respectively, which may be attributed to oxygenated moieties for

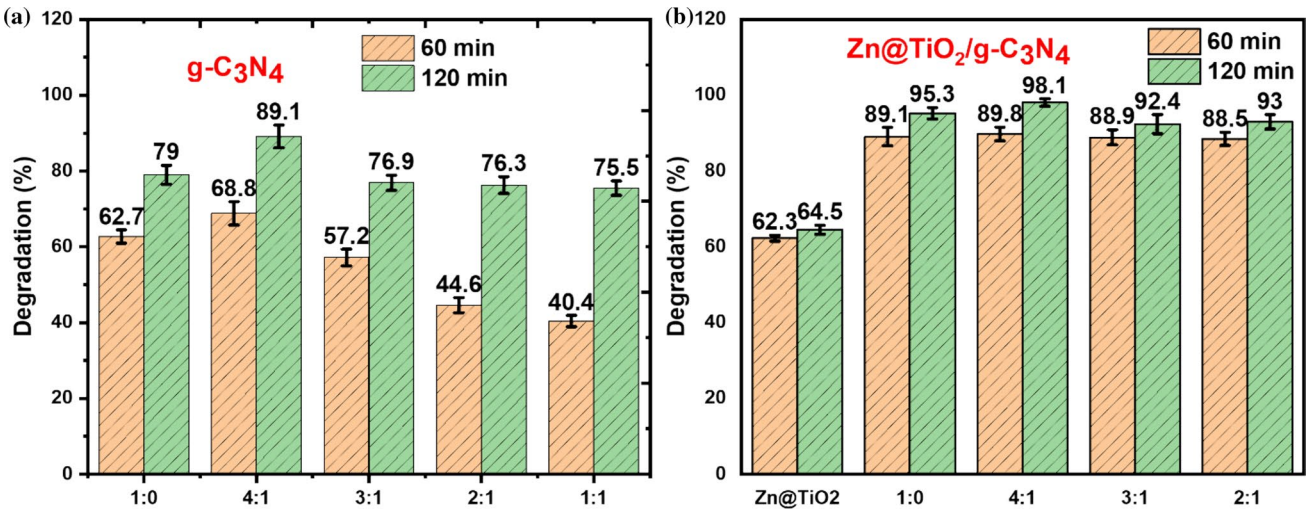

Figure 7 Dye degradation (%) by **a** only g-C_3N_4 after 60 minutes (yellow) and after 120 minutes (green), and **b** by doped Zn@TiO_2, and Zn@TiO_2/g-C_3N_4.

dye adsorption, optimised surface defects and porosity for charge carrier separation, and generation of reactive ROS ($HO^{\bullet}$ and $O_2^{\bullet-}$) for dye degradation.

Fig. 7-b shows dye degradation by Zn@TiO_2 and composites of Zn@TiO_2 with defected g-C_3N_4 which analyses effect of integration of doped metal oxide (Zn@TiO_2) with g-C_3N_4. Pure Zn@ TiO_2 alone achieved 62 % methylene blue degradation after 60 min and 64.5 % after 120 min under identical sunlight conditions (Fig. 7-b). This moderate activity confirms that Zn doping extends the visible-light response of TiO_2, yet the performance remains substantially lower than that of the Zn@TiO_2/g-C_3N_4 heterojunctions, underscoring the synergistic benefit of coupling with defect-engineered g-C_3N_4. All composite catalysts showed higher degradation than g-C_3N_4 due to the formation of a heterojunction between Zn@TiO_2 and g-C_3N_4 which lowers the bandgap to capture visible light and leads to the formation of higher numbers of reactive ROS and efficient dye degradation. Moreover, composite catalysts of Zn@TiO_2/g-C_3N_4 also showed similar trend of decreasing degradation with increasing oxygenated defects by cyanuric acid where Zn@TiO_2/g-C_3N_4 (4:1) showed highest degradation of 89.8 % and 98.5 % at 60 min and 120 min, respectively, due to optimum defect generation while g-C_3N_4 (1:1) showed lowest degradation of 75.6 % and 86 % at 60 min and 120 min, respectively, due to cyanuric acid aided massive defects as charge traps with limited ROS generation for dye degradation.

The dye degradation increased for longer time with 1.5–2-fold increase when irradiation time increased from 60 to 120 minutes for g-C_3N_4 and composite Zn@TiO_2/g-C_3N_4 (7-a,b), reflecting sustained ROS ($HO^{\bullet}$ and $O_2^{\bullet-}$) generation under prolonged irradiation. Based on these results, composite Zn@TiO_2/g-C_3N_4 (1:0) as baseline GCN and composite Zn@TiO_2/g-C_3N_4 (4:1) with optimal oxygenated defects showing the highest degradation of 98.1% were selected for further comparative analyses, including dye degradation profiles, effect of different parameters (pH, catalyst dose, time), reusability, mechanical properties, and antibacterial activity for scalable textile wastewater remediation.

The intense peak at 664 nm corresponds to the $\pi \rightarrow \pi^*$ transition of the MB chromophore (heterocyclic thiazine ring). This characteristic peak absorbance intensity reduces with irradiation time for both composites of Zn@TiO_2/g-C_3N_4 (1:0), as shown in Fig. 8-a and Zn@TiO_2/g-C_3N_4 (4:1) as shown in Fig. 8-b. The Zn@TiO_2/g-C_3N_4 (4:1) showed quicker degradation with almost flat absorbance after 150 minutes that can be ascribed to incorporation of oxygen and leads to different degradation mechanisms, which will be explained in detail in later sections.

To offer a semi-quantitative interpretation of the interfacial charge transfer pathway, the conduction

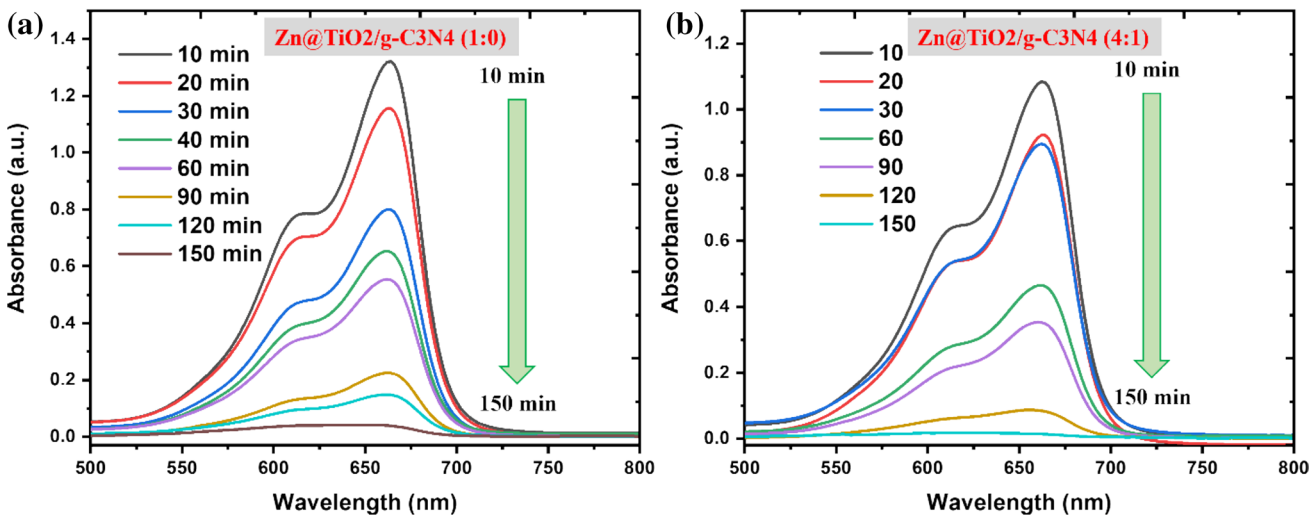

Figure 8 Temporal UV-Vis absorption spectra of methylene blue (MB) degradation under sunlight using **a** Zn@TiO_2/g-C_3N_4 (1:0) and **b** Zn@TiO_2/g-C_3N_4 (4:1) photocatalysts. Reaction conditions: 40 mg catalyst, 100 mL of 10 ppm MB, pH ~6.5, solar irradiance 1000 ± 100 W/m^2 (88000 ± 3000 Lux).

band and valence band edge potentials of defect-tuned g-C_3N_4 and Zn-doped TiO_2 were estimated using the absolute electronegativity relationships.

$$E_{CB} = \chi - E_e - 0.5E_g \quad (2)$$

$$E_{VB} = E_{CB} + E_g \quad (3)$$

where χ is the semiconductor electronegativity, E_e is the energy of free electrons on the hydrogen scale, taken as approximately 4.5 eV, and E_g is the bandgap energy. Electronegativity values of approximately 4.5 and 5.78 eV were considered for defected g-C_3N_4 and the Zn-doped TiO_2 host, respectively. The relatively negative conduction band position (estimated at −1.35 V) of defected g-C_3N_4 provides the reduction potential required for oxygen activation, whereas the more positive valence band position (estimated at +2.68 V) of Zn-doped TiO_2 provides stronger oxidative ability. Consequently, a literature-supported S-scheme-like pathway is proposed in which interfacial recombination of the relatively weak charge carriers retains electrons with stronger reduction potential in the g-C_3N_4 conduction band and holes with stronger oxidation potential in the Zn-doped TiO_2 valence band [62]. Such an arrangement can promote ROS generation while maintaining effective spatial charge separation.

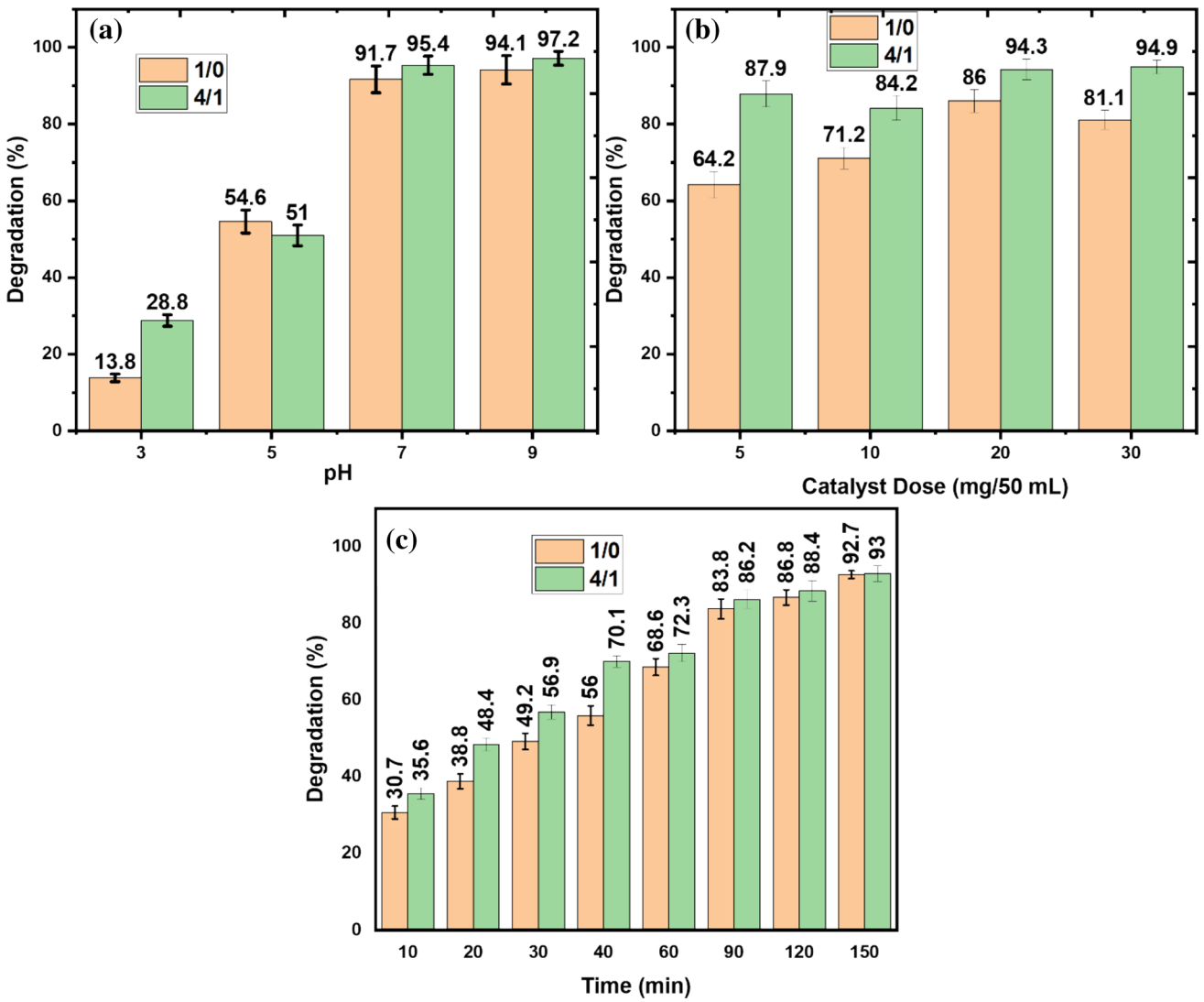

Figure 9 Effect of parameters of **a** pH, **b** catalyst dose, and **c** irradiation time on photodegradation of MB dye.

Effect of parameters on photodegradation

There exists a strong correlation between solution pH, dye structure, and surface charge of adsorbent material for effective photocatalysis [63]. The pH level of dye solution also effects generation of hydroxyl radicals for oxidative photocatalysis. The degradation percentage of MB dye was examined for Zn@TiO_2/g-C_3N_4 (1:0) and Zn@TiO_2/g-C_3N_4 (4:1) at a range of solution pH (3–9) while other factors were kept constant. The effect of initial dye solution pH on the photocatalytic performance of the composite catalyst is shown in Fig. 9-a. The surface charge of the composite photocatalyst facilitates the adsorption of MB dye. At acidic pH, the photocatalyst surface is positively charged, causing electrostatic repulsion with cationic MB^+ and lower degradation %. The degradation was 14 % and 54 % at acidic pH of 3 and 5, respectively, for 1:0 composite catalyst and was 28 % and 51 % at acidic pH of 3 and 5, respectively, for 4:1 composite catalyst. As pH increases to neutral 7 and basic 9, it offers the optimal balance where the negative surface charge of the catalyst maximises MB^+ adsorption while sufficient OH^- ensures high $HO^\bullet$ radical yield, favouring higher adsorption and degradation. The sharp increase in degradation of 92 % at pH 7 was observed for 1:0 composite catalyst, followed by a minimal increase to 94 % at pH 9. The degradation also increased sharply to 95 % at pH 7 for 4:1 composite catalyst, followed by a minimal increase to 97 % at pH 9. The increased photodegradation of Zn@TiO_2/g-C_3N_4 (4:1) (97%) compared to Zn@TiO_2/g-C_3N_4 (1:0) (94 %) can be attributed to –OH functionalities introduced by cyanuric acid to the surface of the catalyst, which can adsorb more MB^+.

The durability of the immobilisation of the photocatalyst is assessed through XRF analysis. Five consecutive photocatalytic cycles were performed under identical sunlight conditions. The fabric retained 91% of its original activity after the fifth cycle. Elemental retention of the immobilised photocatalyst was evaluated by XRF analysis of the coated fabric before and after repeated photocatalytic treatment. The substantial reduction in the peak of Ti of about 16.7% after 5 cycles indicates that the catalyst is largely immobilised, but mechanical stress causes the fibres and photocatalyst to shed off the surface.

The effect of catalyst dosage was systematically investigated to establish the optimum loading for maximum photonic efficiency while avoiding agglomeration-induced shielding. As illustrated in Fig. 9-b, the two composites exhibited markedly different dose–response profiles, underscoring the pivotal role of cyanuric acid-induced oxygenation. For the Zn@TiO_2/g-C_3N_4 (1:0) composite, degradation efficiency increased linearly from 64.2 % at 5 mg to a maximum of 86 % at 20 mg, beyond which a sharp decline to 81 % was observed at 30 mg. This classic behaviour is attributed to particle agglomeration at higher loadings and light-screening, where suspension turbidity reduces photon penetration to inner catalytic sites [64]. In stark contrast, the oxygenated Zn@TiO_2/g-C_3N_4 (4:1) displayed superior performance across the entire dosage range. At the lowest loading of 5 mg, it achieved 88 % degradation, which is 24 % higher than the 1:0 counterpart and can be attributed to enhanced MB^+ adsorption on the oxygen-rich surface. The degradation efficiency peaked at 94.8 % at 30 mg, and such exceptional tolerance to high loading is ascribed to abundant surface -OH groups, which create a hydration shell that prevents agglomeration. The dye degradation process is time dependent which increases with increase in irradiation time [65, 66]. The kinetic profiles (shown in Fig. 9-c) reveal continuous dye degradation and unequivocally demonstrate the faster sunlight-harvesting capability of the oxygenated Zn@TiO_2/g-C_3N_4 (4:1) composite. The dye degradation was quite high in the first 90 minutes, with > 84 % degradation, after which the degradation process slowed down and reached a maximum of 93 % at 150 minutes, where further irradiation time did not affect degradation.

Kinetic study and dyes photodegradation mechanism

Figure 10 presents the kinetic analysis of methylene blue degradation over the Zn@TiO_2/g-C_3N_4 composites. Panels (a) and (c) show the linear plots of ln (C_o/C_t) versus time corresponding to the pseudo-first-order model for the 1:0 and 4:1 composites, respectively, while panels (b) and (d) display the linear plots of ($1/C_t - 1/C_o$) versus time corresponding to the second-order kinetic model for the same catalysts. The R^2 values and K_1 and K_2 constants calculated from the slope of first- and second-order kinetics are given in Table 1. Both composites showed first-order kinetic models because both composites showed the best R^2 value for the first-order model compared to second-order model [26]. The constant K_1 of 0.27/min for Zn@TiO_2/g-C_3N_4 (4:1) composite further supports the

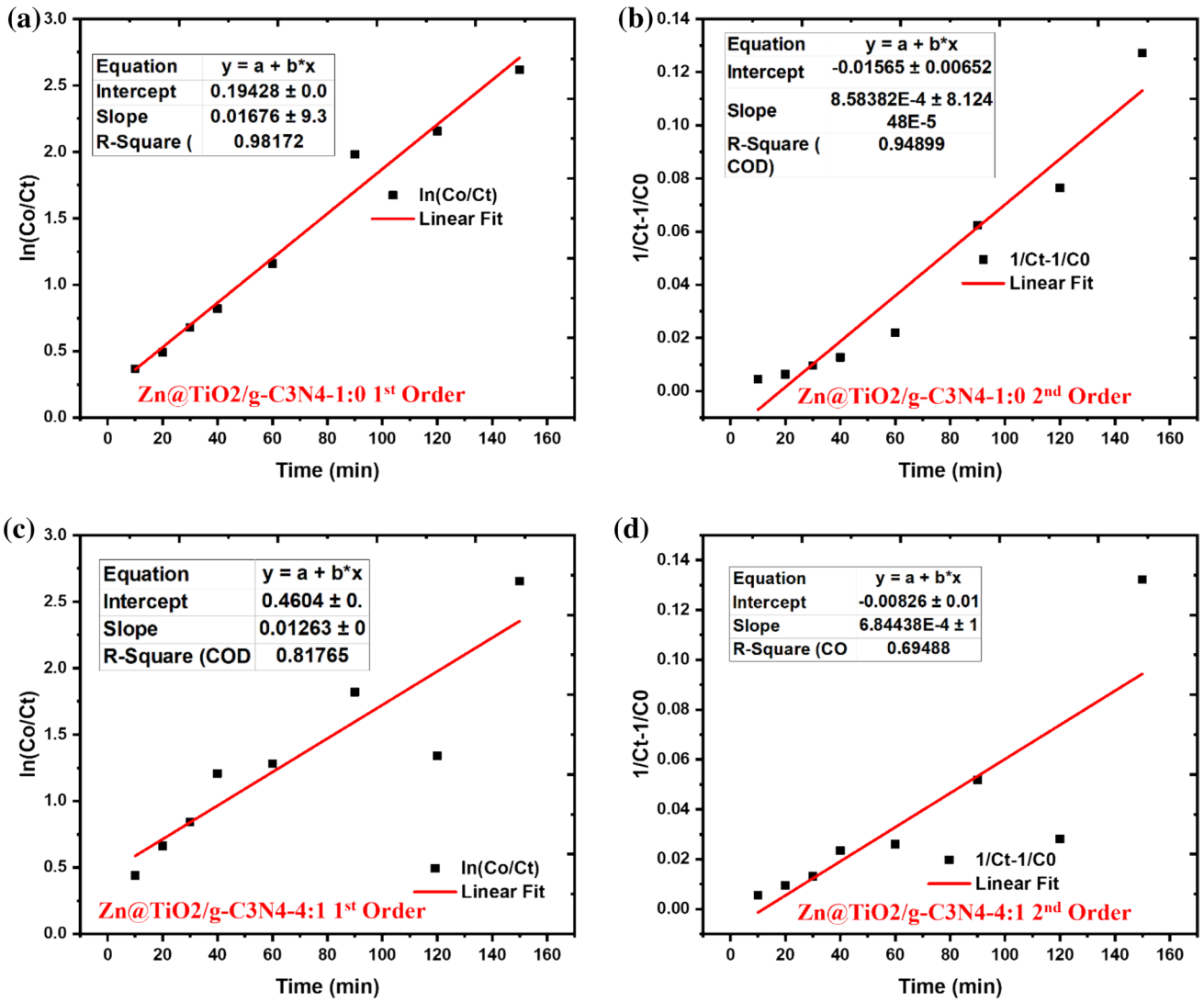

Figure 10 Kinetic study: **a**, **c** first-order, and **b**, **d** second-order reaction kinetic models for 1:0 **a**,**b** and 4:1 composite by using MB dye.

Table 1 Calculated reaction rate constants of 1:0 and 4:1 composite of Zn@TiO_2/g-C_3N_4 towards photodegradation of MB

Composite	First-order kinetics		Second-order kinetics	
	R^2	K_1 (min^{-1})	R^2	K_2 (L $\mu mol^{-1} min^{-1}$)
1:0	0.98	0.0168	0.94	0.0009
4:1	0.87	0.2679	0.69	0.0007

faster dye degradation compared to Zn@TiO_2/g-C_3N_4 (1:0) composite with K_1 of 0.017/min. This trend is also confirmed by Fig. 9-c, which shows a sharp degradation profile, and by Fig. 8-b, where MB absorbance decreases sharply for Zn@TiO_2/g-C_3N_4 (4:1) composite.

Despite the promising performance of the present Zn@TiO_2/defect-engineered g-C_3N_4 heterojunction, several critical challenges remain for Zn-doped TiO_2-based photocatalysts that warrant further attention. First, the long-term photostability of Zn dopants under continuous solar irradiation and fluctuating pH conditions still requires systematic evaluation, as gradual leaching or segregation of Zn^{2+} can diminish visible-light activity over extended operation. Second, precise control of Zn doping concentration and its spatial distribution within the TiO_2 lattice remains difficult; excessive doping often introduces

recombination centres, while insufficient doping fails to optimally narrow the bandgap. Third, scalable and energy-efficient synthesis routes that simultaneously achieve high crystallinity, controlled defect density, and intimate interfacial contact with co-catalysts (such as g-C_3N_4) are still limited. From an application perspective, the transition from powder suspensions to robust, immobilised systems (as demonstrated here on cotton fabric) opens important opportunities. Future research should focus on (i) operando spectroscopic studies to elucidate real-time charge transfer dynamics at the Zn@ TiO_2/g-C_3N_4 interface, (ii) machine learning-assisted optimisation of dopant levels and heterojunction architectures, and (iii) pilot-scale continuous-flow reactors that exploit sunlight-driven, fabric-immobilised photocatalysts for real textile wastewater treatment. Addressing these challenges will accelerate the practical deployment of Zn-doped TiO_2-based materials in sustainable environmental remediation technologies.

The scavenging results were further interpreted in combination with the estimated band alignment to clarify the ROS generation pathway. The calculated CB and VB potentials of defect-modified g-C_3N_4 were approximately −1.35 and +1.35 V vs NHE, respectively, whereas those of Zn-doped TiO_2 were estimated at −0.12 and +2.68 V vs NHE. These band positions favour a proposed S-scheme-like charge transfer pathway, since interfacial recombination of the comparatively weak Zn-doped TiO_2 CB electrons with g-C_3N_4 VB holes would retain strongly reducing electrons on the g-C_3N_4 CB and strongly oxidising holes on the Zn-doped TiO_2 VB. The retained electrons can reduce dissolved O_2 to $\bullet O_2^-$ and subsequently generate H_2O_2/•OH through sequential oxygen reduction reactions, whereas the retained holes can independently oxidise surface H_2O/OH^- to •OH. This dual origin of •OH explains the scavenging response: electron trapping by $K_2Cr_2O_7$ reduced degradation to 88.1% by suppressing the oxygen reduction pathway, while hole trapping by EDTA reduced it to 85.6% by suppressing the oxidative pathway; however, either complementary pathway remained available for ROS generation. In contrast, DMSO directly scavenged the downstream •OH species generated from both pathways and therefore caused a substantially greater decrease in degradation to 60.7%. Accordingly, the results indicate that •OH is the predominant reactive species, while photogenerated electrons and holes serve as essential upstream precursors for its generation rather than being negligible contributors. The proposed MB degradation mechanism is based on an S-scheme heterojunction between defect-tuned g-C_3N_4 and Zn-doped TiO_2. Under sunlight irradiation, photogenerated electrons in the conduction band of Zn-doped TiO_2 recombine with holes in the valence band of g-C_3N_4, retaining strongly reducing electrons in the conduction band of g-C_3N_4 and strongly oxidising holes in the valence band of Zn-doped TiO_2. The retained electrons reduce dissolved O_2 to reactive oxygen species, while the holes oxidise

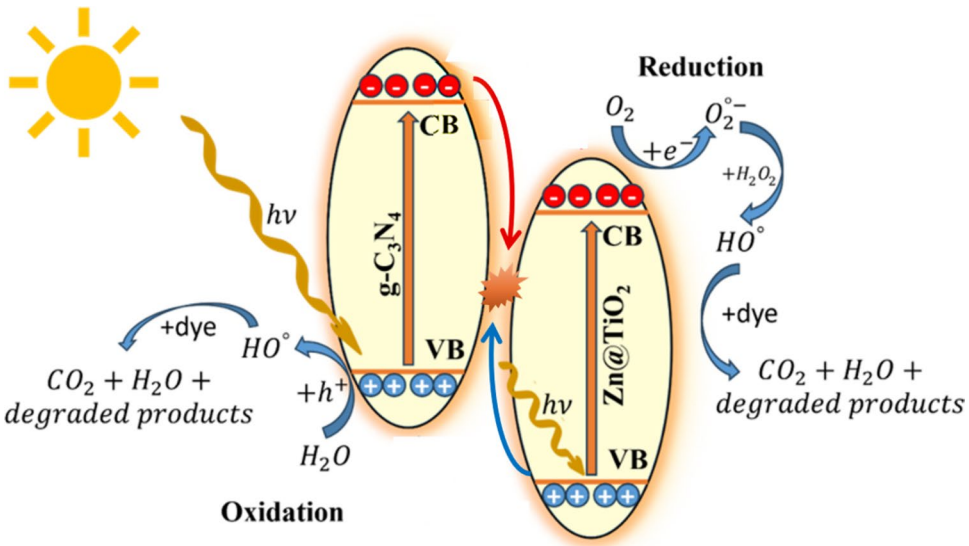

Figure 11 Mechanism of MB dye photocatalytic degradation under visible light by composite of Zn@ TiO_2/g-C_3N_4 due to hydroxyl radicals ($HO^\bullet$).

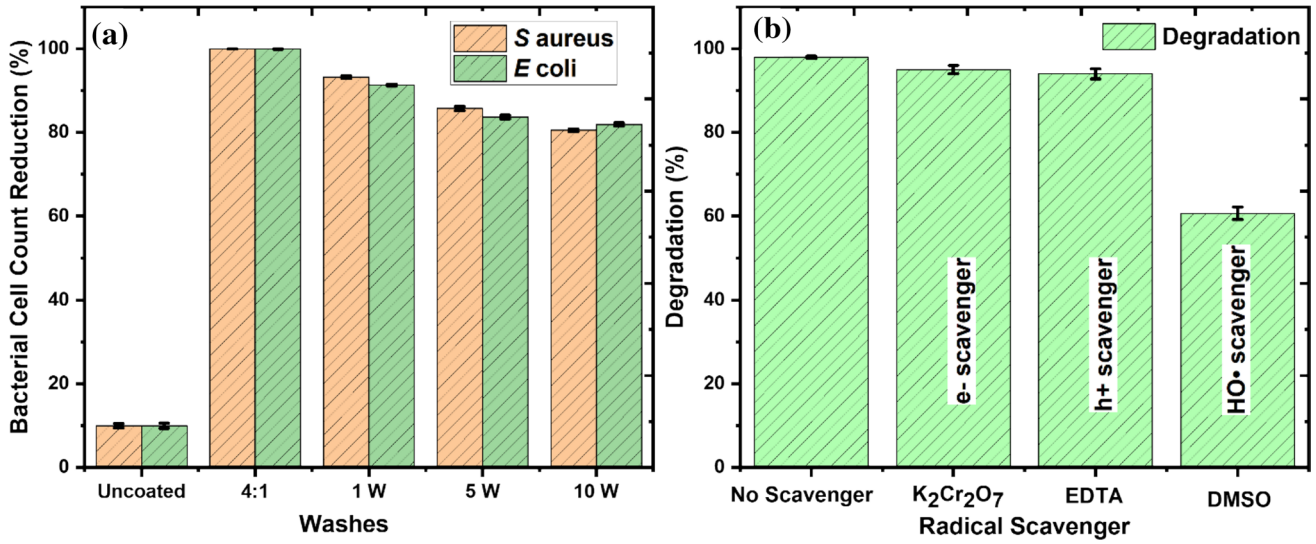

Figure 12 **a** Effect on antimicrobial activity of uncoated and 4:1-coated fabric for after different washing cycles and **b** radical scavenging experiment with scavengers of $K_2Cr_2O_7$, EDTA, and DMSO.

H_2O/OH^- to generate •OH radicals. These reactive species, particularly •OH, subsequently contribute to MB degradation, as illustrated in Fig. 11.

Electrons/holes are generated upon visible-light (with hv > Eg) exposure as shown in Eq. (4).

$$Zn - TiO_2/g - C_3N_4 + hv \rightarrow e^- + h^+ \quad (4)$$

After S-scheme-like interfacial carrier redistribution:

$$e^-_{CB,Zn-TiO2} + h^+_{VB,g-C_3N_4} \rightarrow \text{interfacial recombination} \quad (5)$$

Electrons reduces oxygen (O_2) to superoxide radical ($O_2^{\bullet -}$) as shown in Eq. (6) and protons (H^+) to generate H_2O_2 as shown in Eq. (7).

$$e^-_{CB}(\text{Zn@TiO}_2) + O_2 \rightarrow O_2^{\bullet -} \quad (6)$$

$$2e^-_{CB}(\text{Zn@TiO}_2) + O_2 + 2H^+ \rightarrow H_2O_2 \quad (7)$$

Superoxide radicals ($O_2^{\bullet -}$) further lead to formation of hydroxyl radicals ($HO^{\bullet}$) as shown in Eq. (8).

$$H_2O_2 + O_2^{\bullet -} \rightarrow HO^{\bullet} + HO^- + O_2 \quad (8)$$

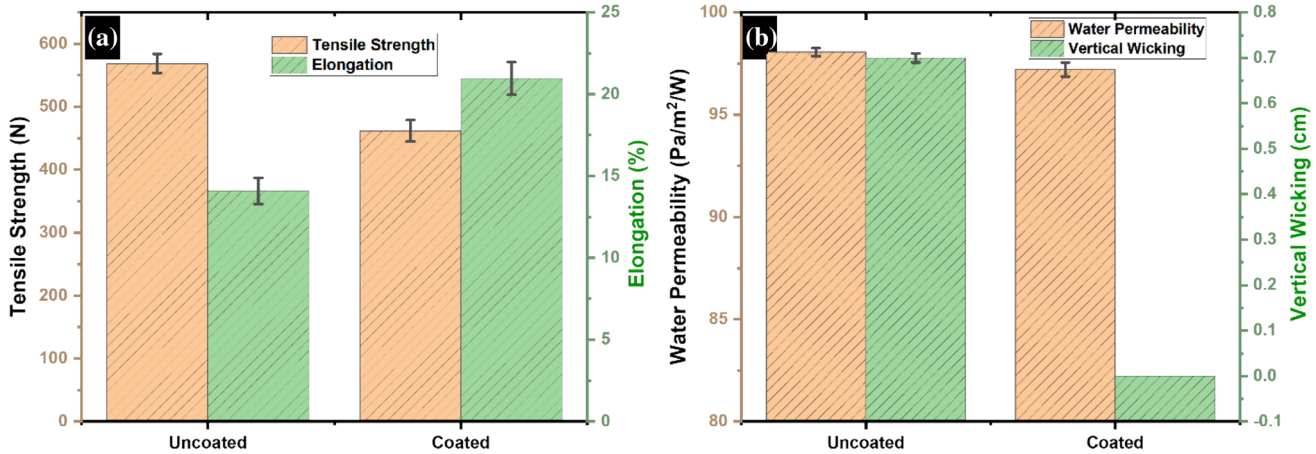

Figure 13 Physical properties of uncoated cotton fabric and Zn@TiO_2/g-C_3N_4-coated cotton fabric **a** tensile strength with % elongation and **b** water permeability and vertical wicking.

The holes at VB of oxidise water (H_2O) and hydroxyl ions (HO^-) to hydroxyl radicals ($HO^\bullet$) as shown in Eq. (9) and (10).

$$h^+_{VB}(g-C_3N_4) + H_2O \rightarrow HO^\bullet + H^+ \quad (9)$$

$$h^+_{VB}(g-C_3N_4) + HO^- \rightarrow HO^\bullet \quad (10)$$

The generated hydroxyl radicals ($HO^\bullet$) interact with MB dye and degrade MB dye to CO_2, H_2O and other degraded products as shown in Eq. (11).

$$HO^\bullet + MBdye \rightarrow CO_2 + H_2O + \text{other degraded products} \quad (11)$$

Antibacterial activity of Zn@TiO2/g-C3N4

The antibacterial potential of Zn@TiO_2/g-C_3N_4 (4:1) composite immobilised onto cotton fabric was evaluated against *Staphylococcus aureus* (Gram-positive) and *Escherichia coli* (Gram-negative). The effect on antimicrobial activity of uncoated and coated fabric is shown in Fig. 12-a. Uncoated fabric was not resistant to *S. aureus* and *E. coli.* The fabric coated with Zn@TiO_2/g-C_3N_4 (4:1) composite showed excellent antibacterial activity, with 99.96% reduction in bacterial cell count. This excellent antibacterial activity may be attributed to enhanced production of ROS ($HO^\bullet$ and $O_2^{\bullet-}$) under visible light, facilitated by Zn-dopant induced bandgap narrowing (~2.8 eV) and the heterojunction with g-C_3N_4, which disrupt bacterial cell membranes and DNA. The coated fabrics after 10 washes showed good antibacterial activity, with a >80% reduction in bacterial cell count. The reduced antibacterial activity might be due to weak nanoparticle adhesion, which may be washed away after multiple washing cycles. However, results suggest that Zn@TiO_2/g-C_3N_4 (4:1)-coated fabric showed promising antibacterial activity.

Physical properties of Zn@TiO_2/g-C_3N_4-coated fabric

The mechanical properties of cotton fabric, both uncoated and coated with the Zn@TiO_2/g-C_3N_4 composite, were evaluated to assess the impact of photocatalytic coating on fabric integrity, as illustrated in Fig. 13 (a). The tensile strength of the uncoated cotton fabric is measured at 569 N, which decreases to 461 N upon coating with Zn@TiO_2/g-C_3N_4 (4:1), representing an 18.8% loss in strength. This reduction is attributed to the potential weakening of inter-fibre bonds or uneven stress distribution introduced by the coating, which may disrupt the fabric's load-bearing structure. The uncoated fabric exhibited an elongation of 14.1%, which increased significantly to 20.96% in the Zn@TiO_2/g-C_3N_4-coated fabric, indicating a 48.8% enhancement. This increase in elongation suggests a plasticising effect from the Zn@TiO_2/g-C_3N_4 (4:1), where the coating acts as a ductile matrix that enhances the fabric's ability to deform under stress, allowing greater extension before failure.

The influence of the Zn@TiO_2/g-C_3N_4 (4:1) coating on the functional properties of vertical wicking and water vapour permeability for the cotton fabric was investigated to evaluate its suitability for textile applications, as shown in Fig. 13 (b). The uncoated cotton fabric exhibited a vertical wicking height of 0.7 cm, which decreases to 0 cm upon coating with Zn@TiO_2/g-C_3N_4 (4:1). This complete loss of wicking ability suggests that the photocatalytic coating formed a barrier layer, likely due to the deposition of Zn@TiO_2/g-C_3N_4 (4:1) nanoparticles, which fill the fabric capillary spaces. Regarding the water vapour permeability index, the uncoated fabric recorded a value of 98.06 $Pa/m^2/W$, which slightly decreased to 97.21 $Pa/m^2/W$ in the coated fabric, indicating a minimal reduction of approximately 0.87%. This negligible change suggests that the Zn@TiO_2/g-C_3N_4 coating, while affecting wicking, preserves the fabric breathability, likely due to the thin, porous nature of the coating layer that allows water vapour diffusion despite the loss of liquid wicking.

Comparison of analogous TiO_2- and g-C_3N_4-based photocatalysts

The following table systematically compares synthesis method, bandgap, degradation efficiency, rate constant, light source and catalyst dosage, thereby positioning the advantages of the integrated defect-tuning by ball milling via fabric-immobilisation strategy developed in this work (Table 2).

The present system uniquely combines defect engineering of g-C_3N_4, Zn-doping of TiO_2, solvent-free ball milling heterojunction formation, and covalent fabric immobilisation, enabling high activity under natural sunlight together with practical recoverability and reusability. The fabric-immobilised catalyst in this work offers a clear practical advantage over powder suspensions reported in many literature studies.

Table 2 Comparison of photocatalytic performance of the present Zn@TiO_2/defect-engineered g-C_3N_4 system with previously reported Zn-doped TiO_2- and g-C_3N_4-based photocatalysts for methylene blue (MB) degradation

Photocatalyst [ref]	Synthesis method	Bandgap (eV)	Degradation efficiency	Rate constant k (min^{-1})	Light source	Catalyst dosage
Zn@ TiO_2/defect-tuned g-C_3N_4 (4:1) on cotton (This work)	Sol–gel + thermal condensation + ex situ ball milling + GPTS immobilisation	~2.8	98 % in 90 min	0.027	Natural sunlight (1000 W m^{-2})	0.4 g L^{-1} (40 mg/100 mL, 10 ppm MB)
Zn@TiO_2 (this study, control)	Sol–gel	~2.8	~62 % in 90 min	–	Natural sunlight (1000 W m^{-2})	0.4 g L^{-1}
Zn-doped TiO_2 (7 mol%) [67]	Green synthesis (plant extract)	3.14	High (MB, sunlight)	Pseudo-first-order (higher than pure TiO_2)	Sunlight	–
Mo/Zn co-doped TiO_2 (7.5 wt% Mo + 2.5 wt% Zn) [68]	Hydrothermal	Narrowed vs. TiO_2	93.8 %	0.0140	Visible light	–
Zn-doped TiO_2 nanostructures [69]	Hydrothermal	Extended to visible	94 % in 30 min	Pseudo-first-order	Visible light	–
g-C_3N_4/TiO_2 nanocomposite [70]	Hydrothermal	–	100 % in 120 min	–	Visible light	–
Tubular g-C_3N_4/TiO_2 S-scheme [62]	Precursor reforming + hydrothermal calcination	–	96.6 % in 60 min	–	Visible light	–
Cellulose/g-C_3N_4/TiO_2 [71]	Eco-friendly immobilisation	–	~95 % in 120 min	–	Natural sunlight	–
TiO_2@ g-C_3N_4 heterostructure [72]	One-step calcination (green)	–	>90 % (various pollutants)	0.014	Visible light	–
g-C_3N_4/TiO_2-ZnO [73]	Calcination/composite formation	Reduced vs. TiO_2	94.6 % (UV)/62.4 % (Vis)	–	UV/Visible	–

Conclusion

This investigation demonstrates the transformative potential of Zn@TiO_2/g-C_3N_4 heterojunction catalysts, synthesised via ball milling with cyanuric acid-optimised oxygenation, as a dual-function powerhouse for solar-driven dye degradation and antibacterial action on cotton fabrics. FTIR, Raman, and XRD results showed successful development of the Zn@TiO_2/g-C_3N_4 composite catalyst. The composite photocatalyst immobilised on cotton fabric achieved 98% MB removal in 90 minutes under ambient sunlight and 99.96% bacterial eradication. The Zn@TiO_2/g-C_3N_4 (4:1) composite photocatalyst outperformed its 1:0 counterpart through controlled defect engineering and enhanced cationic dye absorption due to -OH moieties via cyanuric acid, enhanced charge separation, and rapid dye degradation, with an almost double rate observed during the kinetic study. The mechanism of dye degradation was explored to be hydroxyl radicals ($HO^{\bullet}$)-dominated ROS for rapid MB dye degradation/decolorisation. Fabric immobilisation preserves breathability (97.21 Pa/m^2/W) and boosts elongation (to 21%), offsetting minor tensile losses, making it ideal for self-cleaning textiles. These findings not only bridge the gap between laboratory-scale photocatalysis and industrial viability but also offer a cost-effective, green pathway to combat textile pollution epidemic.

Funding

This project is supported by a HEC Technology Development Fund project grant no. TDF 04-327.

Data availability

Data will be made available on special request.

Declarations

Conflict of interest The authors declare that they have no known conflict of interest that could have appeared to influence the work reported in this paper.

References

[1] UNEP (2025) Unsustainable fashion and textiles in focus for International Day of Zero Waste. Available: https://www.unep.org/news-and-stories/press-release/unsustainable-fashion-and-textiles-focus-international-day-zero. Accessed: 23 Sep 2025 [Online]

[2] Wolfe Isobella, Textile dyes pollution: the truth about fashion's toxic colours, in the know. Available: https://goodonyou.eco/textile-dyes-pollution/#. Accessed: 23 Sep 2025 [Online]

[3] Shanker U, Rani M, Jassal V (2017) Degradation of hazardous organic dyes in water by nanomaterials. Environ Chem Lett 15:623–642. https://doi.org/10.1007/S10311-017-0650-2/METRICS

[4] Fast fashion: EU laws for sustainable textile consumption |Topics| European parliament. Available: https://www.europarl.europa.eu/topics/en/article/20201208STO93327/fast-fashion-eu-laws-for-sustainable-textile-consumption. Accessed: 23 Sep 2025 [Online]

[5] Geneva Environmental Network, Environmental Sustainability in the Fashion Industry—Geneva Environment Network. Available: https://www.genevaenvironmentnetwork.org/resources/updates/sustainable-fashion/. Accessed: 23 Sep 2025 [Online]

[6] Green fashion: Why dyeing clothes has a big environmental impact, BBC. Available: https://www.bbc.com/news/articles/c870j92p82wo. Accessed: 23 Sep 2025 [Online]

[7] Farhan Hanafi M, Sapawe N (2020) A review on the water problem associate with organic pollutants derived from phenol, methyl orange, and remazol brilliant blue dyes. Mater Today Proc 31:A141–A150. https://doi.org/10.1016/j.matpr.2021.01.258

[8] Chung KT (2016) Azo dyes and human health: a review. J Environ Sci Health C Environ Carcinog Ecotoxicol Rev 34:233–261. https://doi.org/10.1080/10590501.2016.1236602

[9] Kataya G et al (2025) Dynamic removal of methylene blue and methyl orange from water using biochar derived from kitchen waste. Sci Rep 15(1):29907. https://doi.org/10.1038/s41598-025-14133-6

[10] Stanescu MD (2021) State of the art of post-consumer textile waste upcycling to reach the zero waste milestone. Environ Sci Pollut Res 28(12):14253–14270. https://doi.org/10.1007/s11356-021-12416-9

[11] Rasool BS, Abbas AK, Haddad R (2025) Photocatalytic innovations in environmental remediation: mechanisms, materials, and challenges for persistent organic pollutant removal. Environ Monit Assess 197(10):1086-. https://doi.org/10.1007/s10661-025-14531-3

[12] Kumar M, Singh VP, Bhat SB, Kumar R (2025) Environmental risks of textile dyes and photocatalytic materials for sustainable treatment: current status and future directions. Discov Environ 3(1):132. https://doi.org/10.1007/s44274-025-00337-0

[13] Al Miad A, Saikat SP, Alam MK, Hossain MS, Bahadur NM, Ahmed S (2024) Metal oxide-based photocatalysts for the efficient degradation of organic pollutants for a sustainable environment: a review. Nanoscale Adv 6(19):4781–4803. https://doi.org/10.1039/d4na00517a

[14] Molla MAI, Ahmed AZ, Kaneco S (2021) Reaction mechanism for photocatalytic degradation of organic pollutants, Nanostruct Photocatal: Fundam Pract Appl: 63–84. https://doi.org/10.1016/B978-0-12-823007-7.00011-0

[15] Opoku F, Govender KK, van Sittert CGCE, Govender PP (2017) Recent progress in the development of semiconductor-based photocatalyst materials for applications in photocatalytic water splitting and degradation of pollutants. Adv Sustain Syst 1:1700006. https://doi.org/10.1002/adsu.201700006

[16] Ahmad Z, Abdullah MK, Ali MZ, Zawawi MAM (2023) Polymers in electronics. Elsevier

[17] Zeshan M et al (2022) Single-step treatment to improve conductivity of PEDOT: PSS by hydrobromic acid solution for application of transparent electrode. Org Electron 110:106643. https://doi.org/10.1016/j.orgel.2022.106643

[18] Ali MZ, Ishak KMK, Zawawi MAM, Jaafar M, Ahmad Z (2022) Simultaneous enhancement of conductivity and Seebeck coefficient of PEDOT:PSS by triflic acid treatment for flexible thermoelectric generator. Synth Met 286:117037. https://doi.org/10.1016/j.synthmet.2022.117037

[19] Chakravorty A, Roy S (2024) A review of photocatalysis, basic principles, processes, and materials. Sustain Chem Environ 8:100155. https://doi.org/10.1016/j.scenv.2024.100155

[20] Tran HD, Nguyen DQ, Do PT, Tran UNP (2023) Kinetics of photocatalytic degradation of organic compounds: a mini-review and new approach. RSC Adv 13:16915–16925. https://doi.org/10.1039/d3ra01970e

[21] Bahrudin NN (2022) Evaluation of degradation kinetic and photostability of immobilized TiO2/activated carbon bilayer photocatalyst for phenol removal. Appl Surf Sci Adv 7:100208. https://doi.org/10.1016/j.apsadv.2021.100208

[22] Molinari R, Lavorato C, Argurio P (2020) Visible-light photocatalysts and their perspectives for building photocatalytic membrane reactors for various liquid phase chemical conversions. Catalysts 10:1–38. https://doi.org/10.3390/catal10111334

[23] Wang Y, Wang X, Antonietti M (2012) Polymeric graphitic carbon nitride as a heterogeneous organocatalyst: from photochemistry to multipurpose catalysis to sustainable chemistry. Angew Chem Int Ed 51:68–89. https://doi.org/10.1002/anie.201101182

[24] Liu X et al (2021) Recent developments of doped g-C3N4 photocatalysts for the degradation of organic pollutants. Crit Rev Environ Sci Technol 51:751–790. https://doi.org/10.1080/10643389.2020.1734433

[25] Rafique M et al (2023) Hydrogen production using TiO2-based photocatalysts: a comprehensive review. ACS Omega 8:25640–25648. https://doi.org/10.1021/acsomega.3c00963

[26] Arfa U et al (2023) Sunlight-driven photocatalytic active fabrics through immobilization of functionalized doped titania nanoparticles. Polymers 15:2775. https://doi.org/10.3390/polym15132775

[27] Linsebigler AL, Lu G, Yates JT (2002) Photocatalysis on TiO2 surfaces: principles, mechanisms, and selected results. Chem Rev 95:735–758. https://doi.org/10.1021/cr00035a013

[28] Fujishima A, Zhang X, Tryk DA (2008) TiO2 photocatalysis and related surface phenomena. Surf Sci Rep 63:515–582. https://doi.org/10.1016/j.surfrep.2008.10.001

[29] Karuppasamy P, Ramzan Nilofar Nisha N, Pugazhendhi A, Kandasamy S, Pitchaimuthu S (2021) An investigation of transition metal doped TiO2 photocatalysts for the enhanced photocatalytic decoloration of methylene blue dye under visible light irradiation. J Environ Chem Eng 9:105254. https://doi.org/10.1016/J.JECE.2021.105254

[30] Rajaitha PM et al (2022) Unraveling highly efficient nanomaterial photocatalyst for pollutant removal: a comprehensive review and future progress. Mater Today Chem 23:100692. https://doi.org/10.1016/J.MTCHEM.2021.100692

[31] Yu X, Ng SF, Putri LK, Tan LL, Mohamed AR, Ong WJ (2021) Point-defect engineering: leveraging imperfections in graphitic carbon nitride (g-C3N4) photocatalysts toward artificial photosynthesis,. Small 17:2006851. https://doi.org/10.1002/smll.202006851

[32] Hou S et al (2024) Decade milestone advancement of defect-engineered g-C3N4 for solar catalytic applications. Nano-Micro Lett 16(1):70. https://doi.org/10.1007/s40820-023-01297-x

[33] Wang X et al (2019) Supramolecular precursor strategy for the synthesis of holey graphitic carbon nitride nanotubes with enhanced photocatalytic hydrogen evolution performance. Nano Res 12(9):2385–2389. https://doi.org/10.1007/s12274-019-2357-0

[34] Cantor Pérez F et al (2025) Comparative thermal and supramolecular hydrothermal synthesis of g-C3N4 toward efficient photocatalytic degradation of gallic acid. Catalysts 15:858

[35] Hu J, Liu H, Sun C, Wu L, Jiao F (2024) Precise defect engineering with ultrathin porous frameworks on g-C3N4 for synergetic boosted photocatalytic hydrogen evolution. Ind Eng Chem Res 63:2665–2675. https://doi.org/10.1021/acs.iecr.3c03794

[36] Shi L et al (2018) Photoassisted construction of holey defective g-C3N4 photocatalysts for efficient visible-light-driven H2O2 production. Small 14:1703142. https://doi.org/10.1002/smll.201703142

[37] Yang Z, Zhang Y, Schnepp Z (2015) Soft and hard templating of graphitic carbon nitride. J Mater Chem A Mater 3:14081–14092. https://doi.org/10.1039/c5ta02156a

[38] Dong J, Zhang Y, Hussain MI, Zhou W, Chen Y, Wang LN (2022) g-C3N4: properties, pore modifications, and photocatalytic applications. Nanomaterials. https://doi.org/10.3390/nano12010121

[39] Cui L et al (2018) Constructing ultrathin g-C3N4 nanosheets with hierarchical pores by NaClO induced wet etching for efficient photocatalytic Cr(VI) detoxification under visible light irradiation. Diamond Relat Mater 88:51–59. https://doi.org/10.1016/j.diamond.2018.06.016

[40] Kumar A, Raizada P, Hosseini-Bandegharaei A, Thakur VK, Nguyen VH, Singh P (2021) C-, N-vacancy defect engineered polymeric carbon nitride towards photocatalysis: viewpoints and challenges. J Mater Chem A Mater 9:111–153. https://doi.org/10.1039/d0ta08384d

[41] Eroglu Z, Ozer MS, Metin Ö (2024) Nitrogen-based imperfections in graphitic carbon nitride—new trend

for enhancing photocatalytic activity? ChemCatChem 16:e202301560. https://doi.org/10.1002/cctc.202301560

[42] Feng Z et al (2020) In situ preparation of g-C3N4/Bi4O5I2 complex and its elevated photoactivity in methyl orange degradation under visible light. J Environ Sci 87:149–162. https://doi.org/10.1016/J.JES.2019.05.032

[43] Zhu Q, Cai Z, Zhou P, Sun X, Xu J (2023) Recent progress of membrane technology for chiral separation: a comprehensive review. Sep Purif Technol 309:123077. https://doi.org/10.1016/J.SEPPUR.2022.123077

[44] Li H et al (2026) Electrically coupled MXene/Co–C3N4 membrane enable dynamic electro-responsive efficient separation. Adv Funct Mater 36:e75584. https://doi.org/10.1002/ADFM.75584;WGROUP:STRING:PUBLICATION

[45] Qi Z, An Z, Huang B, Wu M, Wu Q, Jiang D (2023) Visible-light-catalyzed synthesis of 1,3-benzoxazines via formal [4 + 2] cycloaddition of oximes with o-hydroxybenzyl alcohols. Org Biomol Chem 21:6419–6423. https://doi.org/10.1039/D3OB00882G

[46] Yang W et al (2025) Synergistic photocatalysis of acridinium salts and pyridine N-oxides for α-aminoalkylation with N-methylsulfonamides. J Org Chem 90:16403–16413. https://doi.org/10.1021/ACS.JOC.5C01813

[47] Zhou J, Zhang M, Zhu Y (2015) Photocatalytic enhancement of hybrid C3N4/TiO2 prepared via ball milling method. Phys Chem Chem Phys 17:3647–3652. https://doi.org/10.1039/C4CP05173D

[48] Zhu K et al (2020) Facile fabrication of ZnPc sensitized g-C3N4 through ball milling method toward an enhanced photocatalytic property. J Asian Ceram Soc 8:939–947. https://doi.org/10.1080/21870764.2020.1799912

[49] Akhtar N et al (2024) Solar light-driven photocatalytic degradation potential of g-C3N4 based binary chalcogenides (AgBiS2/g-C3N4). Mater Chem Phys 316:129067. https://doi.org/10.1016/j.matchemphys.2024.129067

[50] Sun J et al (2025) A single-atom manganese nanozyme mediated membrane reactor for water decontamination. Water Res 268:122627. https://doi.org/10.1016/J.WATRES.2024.122627

[51] Xie M et al (2026) Multiscale thermodynamic insights into membrane fouling control by biochar-activated peroxymonosulfate pretreatment: synergy of oxidation and adsorption. Water Res 288:124564. https://doi.org/10.1016/J.WATRES.2025.124564

[52] Wu M et al (2023) High propensity of membrane fouling and the underlying mechanisms in a membrane bioreactor during occurrence of sludge bulking. Water Res 229:119456. https://doi.org/10.1016/J.WATRES.2022.119456

[53] Yao X, Li R, Shen L, Zhao L, Lin H (2025) A novel magnetically induced Co@NC-modified electrochemical membrane for continuous peroxymonosulfate activation: achieving ultrafast and cost-effective purification with elucidation of mechanism and application potential. Water Res 287:124436. https://doi.org/10.1016/J.WATRES.2025.124436

[54] Wang J, Wang H, Shen L, Li R, Lin H (2023) A sustainable solution for organic pollutant degradation: novel polyethersulfone/carbon cloth/FeOCl composite membranes with electric field-assisted persulfate activation. Water Res 244:120530. https://doi.org/10.1016/J.WATRES.2023.120530

[55] Nie L et al (2021) Polyphenol rich green tea waste hydrogel for removal of copper and chromium ions from aqueous solution. Clean Eng Technol 4:100167. https://doi.org/10.1016/J.CLET.2021.100167

[56] Praus P, Smýkalová A, Foniok K, Novák V, Hrbác J (2021) Doping of graphitic carbon nitride with oxygen by means of cyanuric acid: Properties and photocatalytic applications. J Environ Chem Eng 9:105498. https://doi.org/10.1016/j.jece.2021.105498

[57] Ohsaka T, Izumi F, Fujiki Y (1978) Raman spectrum of anatase, TiO2. J Raman Spectrosc 7:321–324. https://doi.org/10.1002/jrs.1250070606

[58] Muhmood T et al (2024) Graphene-like graphitic carbon nitride (g-C3N4) as a semiconductor photocatalyst: Properties, classification, and defects engineering approaches. Mater Today Sustain 25:100633. https://doi.org/10.1016/J.MTSUST.2023.100633

[59] Jiang J et al (2014) Dependence of electronic structure of g-C3N4 on the layer number of its nanosheets: a study by Raman spectroscopy coupled with first-principles calculations. Carbon 80:213–221. https://doi.org/10.1016/J.CARBON.2014.08.059

[60] Liu J, Wang H, Antonietti M (2016) Graphitic carbon nitride 'reloaded': emerging applications beyond (photo) catalysis. Chem Soc Rev 45:2308–2326. https://doi.org/10.1039/c5cs00767d

[61] Arfa U et al (2023) Sunlight-driven photocatalytic active fabrics through immobilization of functionalized doped titania nanoparticles. Polymers (Basel) 15:2775. https://doi.org/10.3390/polym15132775

[62] Wang J et al (2023) Construction of tubular g-C3N4/TiO2 S-scheme photocatalyst for high-efficiency degradation of organic pollutants under visible light. J Alloys Compd 947:169659. https://doi.org/10.1016/J.JALLCOM.2023.169659

[63] Lachheb H et al (2002) Photocatalytic degradation of various types of dyes (Alizarin S, Crocein Orange G, Methyl

Red, Congo Red, Methylene Blue) in water by UV-irradiated titania. Appl Catal B Environ 39:75–90. https://doi.org/10.1016/S0926-3373(02)00078-4

[64] Neppolian B, Choi HC, Sakthivel S, Arabindoo B, Murugesan V (2002) Solar light induced and TiO2 assisted degradation of textile dye reactive blue 4. Chemosphere 46:1173–1181. https://doi.org/10.1016/S0045-6535(01)00284-3

[65] Fan J, Hu X, Xie Z, Zhang K, Wang J (2012) Photocatalytic degradation of azo dye by novel Bi-based photocatalyst Bi4TaO8I under visible-light irradiation. Chem Eng J 179:44–51. https://doi.org/10.1016/J.CEJ.2011.10.029

[66] Konstantinou IK, Albanis TA (2004) TiO2-assisted photocatalytic degradation of azo dyes in aqueous solution: kinetic and mechanistic investigations: a review. Appl Catal B 49:1–14. https://doi.org/10.1016/J.APCATB.2003.11.010

[67] Abduh NAY, Algarni TS, Al-Odayni AB (2024) Green synthesis of Zn-doped TiO2 nanomaterials for photocatalytic degradation of crystal violet and methylene blue dyes under sunlight. Biomass Convers Biorefinery 15:4849–4865. https://doi.org/10.1007/S13399-024-06120-0

[68] Ijaz M et al (2026) Synergistic effects of Mo and Zn in TiO2 for photocatalytic degradation of methylene blue. J Iran Chem Soc 23:129. https://doi.org/10.1007/S13738-026-03432-Y

[69] Santhi K, Ponnusamy S, Harish S, Navaneethan M (2022) A facile synthesis of Zn-doped TiO2 nanostructures for enhanced photocatalytic performance. J Mater Sci Mater Electron 33:9798–9813. https://doi.org/10.1007/S10854-022-07945-Z

[70] Razali MH, MdFauzi MAF, MohdAzam B, Yusoff M (2022) g-C3N4/TiO2 nanocomposite photocatalyst for methylene blue photodegradation under visible light. Appl Nanosci 12:3197–3206. https://doi.org/10.1007/S13204-021-02328-Y

[71] Garg A et al (2023) Sunlight active cellulose/g-C3N4/TiO2 nano-photocatalyst for simultaneous degradation of methylene blue dye and atenolol drug in real wastewater. Nanotechnology 34:505705. https://doi.org/10.1088/1361-6528/ACF9AD

[72] Xiao G, Xu S, Li P, Su H (2018) Visible-light-driven activity and synergistic mechanism of TiO2@g-C3N4 heterostructured photocatalysts fabricated through a facile and green procedure for various toxic pollutants removal. Nanotechnology 29:315601. https://doi.org/10.1088/1361-6528/AAC304

[73] Saeidpour S, Khoshnevisan B, Boroumand Z (2022) Synthesis and characterization of a g-C3N4/TiO2-ZnO nanostructure for photocatalytic degradation of methylene blue. Nano Futures 6:035001. https://doi.org/10.1088/2399-1984/AC74FA